

# Modelling of the HG-A Experiment (FORGE WP 4.3)

**NWMO TR-2014-07**

**September 2014**

**Robert Walsh, Othman Nasir and Nicholas Sgro**

Geofirma Engineering Ltd.

**nwmo**

NUCLEAR WASTE  
MANAGEMENT  
ORGANIZATION

SOCIÉTÉ DE GESTION  
DES DÉCHETS  
NUCLÉAIRES

**Nuclear Waste Management Organization**

22 St. Clair Avenue East, 6<sup>th</sup> Floor

Toronto, Ontario

M4T 2S3

Canada

Tel: 416-934-9814

Web: [www.nwmo.ca](http://www.nwmo.ca)

## **Modelling of the HG-A Experiment (FORGE WP 4.3)**

**NWMO TR-2014-07**

September 2014

**Robert Walsh, Othman Nasir and Nicholas Sgro**  
Geofirma Engineering Ltd.

This report has been prepared under contract to NWMO. The report has been reviewed by NWMO, but the views and conclusions are those of the authors and do not necessarily represent those of the NWMO.

All copyright and intellectual property rights belong to NWMO.

**Document History**

Title:	Modelling of the HG-A Experiment (FORGE WP 4.3)		
Report Number:	NWMO TR-2014-07		
Revision:	R000	Date:	September 2014
Geofirma Engineering Ltd.			
Authored by:	Robert Walsh, Othman Nasir and Nicholas Sgro		
Verified by:	Nicola Calder and John Avis		
Approved by:	John Avis		
Nuclear Waste Management Organization			
Reviewed by:	Helen Leung and Erik Kremer		
Accepted by:	Paul Gierszewski		

## ABSTRACT

**Title:** Modelling of the HG-A Experiment (FORGE WP 4.3)  
**Report No.:** NWMO TR-2014-07  
**Author(s):** Robert Walsh, Othman Nasir and Nicholas Sgro  
**Company:** Geofirma Engineering Ltd.  
**Date:** September 2014

### Abstract

This technical report documents the work of Geofirma Engineering on modelling the HG-A field experiment at Mont Terri underground research laboratory in Switzerland as part of FORGE (Fate of Repository Gases) WP 4.3 for the Nuclear Waste Management Organization (NWMO). The HG-A test examined gas and water flow in the Excavation Damage Zone (EDZ) of a tunnel in Opalinus clay. It was intended to examine the long-term leakage of gas from a small, backfilled and sealed tunnel, and to identify the location and properties of gas release pathways in very low permeability host rock. The experiment was divided into four stages: the multi-rate hydraulic test, Gas Test 1, Gas Test 2 and Gas Test 3. It provided substantial evidence for large EDZ permeability changes, particularly during the multi-rate hydraulic test. Apparent EDZ permeability was likely affected by three processes: (1) swelling of the damaged rock in the presence of water and subsequent healing of fractures causing a steady reduction in the permeability of the EDZ; (2) hydromechanical coupling as changes in pore pressure and confining stress led to changes in EDZ permeability; and (3) leakage of fluids along the packer-rock interface caused by low effective stress.

This report is divided into two sections: (1) multiphase flow modelling and (2) hydromechanical coupled modelling. The multiphase flow modelling used T2GGM, a code that couples TOUGH2 multi-phase flow code with the Gas Generation Model, GGM. To reproduce the experimental results of the multi-rate hydraulic test using T2GGM, we used a time-variable EDZ permeability, which required a new algorithm to be added to T2GGM. This approach was very successful in modelling the pressure measurements in the HG-A test section. Modelling of the gas injection tests using T2GGM did not require large changes in EDZ permeability and was similarly successful, indicating that the EDZ properties were stabilizing.

Although the T2GGM models successfully reproduced observed pressures, they could not directly model the mechanical processes governing EDZ permeability. To consider mechanical processes, we developed T2GGM-FLAC, which couples T2GGM and FLAC3D. Two-phase flow is simulated in T2GGM, while mechanical processes are handled by FLAC3D. This coupled model was used to predict the development of excavation damage around the HG-A tunnel, and then model the EDZ permeability variation as a function of time (self sealing) and packer pressure (hydromechanical coupling). EDZ development was predicted based on plastic deformation and permeability was modified as a function of damage. The distribution of damage around the HG-A tunnel predicted by the model corresponded well to available measurements of damage from laser scans of the tunnel walls post-excavation. This qualitative fit was not a result of careful calibration, but rather the application of geomechanical first principles, laboratory measurements of geomechanical parameters, and estimates of the local rock stress state. Calculating the damage-induced permeability required calibration of a number of empirical parameters. With limited calibration, this approach was able to reproduce measured test zone pressures with reasonable accuracy.



## TABLE OF CONTENTS

	<u>Page</u>
<b>ABSTRACT .....</b>	<b>iii</b>
<b>1. INTRODUCTION .....</b>	<b>1</b>
<b>2. EXPERIMENTAL DATA SET .....</b>	<b>3</b>
<b>3. TWO-PHASE FLOW MODELLING .....</b>	<b>9</b>
<b>3.1 CODE USED .....</b>	<b>9</b>
<b>3.2 MODEL SETUP .....</b>	<b>9</b>
3.2.1 2D Radial Hydraulic Model .....	9
3.2.1.1 Boundary Conditions .....	11
3.2.1.2 Initial Conditions .....	11
3.2.1.3 Source Term .....	13
3.2.1.4 Time Varying Permeability .....	13
3.2.2 3D Radial Hydraulic Model .....	15
3.2.2.1 Properties .....	16
3.2.2.2 Boundary Conditions .....	19
3.2.2.3 Initial Conditions .....	20
3.2.2.4 Source Term .....	20
<b>3.3 RESULTS AND DISCUSSION FOR 2D AND 3D MODELS .....</b>	<b>21</b>
3.3.1 2D Model Results .....	21
3.3.1.1 Water Flow Model: Constant EDZ Permeability .....	21
3.3.1.2 Water Flow Model: Variable EDZ Permeability .....	22
3.3.2 3D Model Results .....	23
3.3.2.1 Hydraulic Test (Water Only) .....	23
3.3.2.2 Gas Test 1 .....	24
3.3.2.3 Gas Test 2 .....	25
3.3.2.4 Gas Test 3 .....	26
3.3.2.5 Gas Flow Discussion .....	28
<b>4. HYDRO-MECHANICAL MODELLING .....</b>	<b>29</b>
<b>4.1 CODE USED .....</b>	<b>29</b>
<b>4.2 CONSTITUTIVE MODELS .....</b>	<b>30</b>
4.2.1 Elasto-Plastic Mechanical Model .....	30
4.2.2 EDZ Damage and Permeability .....	34
4.2.3 EDZ Swelling and Permeability .....	35
4.2.4 Packer Interface Permeability and Boundary Conditions .....	36
<b>4.3 MODEL SETUP .....</b>	<b>38</b>
4.3.1 Properties .....	38
4.3.2 Model Geometry and Property Distribution .....	40
4.3.3 Initial and Boundary Conditions .....	41
<b>4.4 RESULTS AND DISCUSSION .....</b>	<b>43</b>
4.4.1 Excavation Damage Zone Development .....	43
4.4.2 Changes in Permeability .....	44
4.4.2.1 EDZ .....	44
4.4.2.2 Packer-Rock Interface .....	45
4.4.3 Test Zone Pressure .....	46

4.4.4	Discussion .....	48
<b>5.</b>	<b>CONCLUSIONS .....</b>	<b>50</b>
	<b>REFERENCES .....</b>	<b>52</b>
	<b>APPENDIX A: SENSOR LOCATIONS .....</b>	<b>55</b>
	<b>APPENDIX B: VAN GENUCHTEN MODEL .....</b>	<b>57</b>

**LIST OF TABLES**

	<b><u>Page</u></b>
Table 3-1: Model Properties for Water Saturated Flow.....	11
Table 3-2: Model Properties for Gas Injection Tests.....	17
Table 3-3: Model Properties for Two-Phase Flow (van Genuchten Properties).....	18
Table 4-1: Failure Mode and Corresponding Estimated Change in Parameter $B$ .....	34
Table 4-2: Properties for the Ubiquitous Joint Model.....	39

**LIST OF FIGURES**

	<b><u>Page</u></b>
Figure 1-1: Layout of the Mont-Terri URL Showing the HG-A Tunnel at the Bottom Right (from Lanyon et al. 2009) .....	2
Figure 1-2: Layout of the HG-A Experiment Showing Piezometers and Total Stress Sensors in the HG-A Tunnel and Surrounding Boreholes .....	2
Figure 2-1: 2D Projection of Sensor Locations at the Interface between the Packer and the Tunnel Wall.....	3
Figure 2-2: Multi-rate Hydraulic Test Data from the HG-A Experiment.....	5
Figure 2-3: 2D Projection of Pore Pressures at the Interface between the Packer and the Tunnel Wall.....	6
Figure 2-4: Damage Zone around Tunnel (a) Schematic Representation and (b) Laser Scans of the Tunnel between 6 and 13 m Depth (from Marschall et al. 2006).....	7
Figure 2-5: Gas Injection Test Data from the HG-A Experiment.....	8
Figure 3-1: 2D-Radial Grid Discretization .....	10
Figure 3-2: 2D-Radial Model Boundary Conditions .....	11
Figure 3-3: 2D-Radial Model Initial Pressure Distribution for the Water Flow Model.....	12
Figure 3-4: Measured Formation Pore Pressures at Time = 0.0 days (Lanyon 2011b).....	12
Figure 3-5: Measured Injection Rates and Flow Rates Used in the Water Flow Model.....	13
Figure 3-6: EDZ Permeability for Water Flow, and Pressure Data Used for Interpretation of the EDZ Permeability.....	15
Figure 3-7: 3-D Model Discretization .....	16
Figure 3-8: 3-D Model Property Distribution .....	17
Figure 3-9: Capillary Pressure and Relative Permeability Curves .....	19
Figure 3-10: 3D-Radial Model Boundary Conditions .....	19
Figure 3-11: 3D-Radial Model Typical Initial Pressure Distribution for the Gas Flow Model (Plan Section View) .....	20
Figure 3-12: Measured Injection Rates and Flow Rates Used in the Gas Flow Models.....	21
Figure 3-13: Measured and Modelled Test Zone Pressures During the Multi-rate Hydraulic Test, Constant EDZ Permeability Models.....	22
Figure 3-14: Measured and Modelled Test Zone Pressures During the Multi-rate Hydraulic Test, 2D Variable EDZ Permeability Model .....	23
Figure 3-15: Measured and Modelled Test Zone Pressures During the Multi-rate Hydraulic Test, 3D Variable EDZ Permeability Model .....	24
Figure 3-16: Measured and Modelled Test Zone and EDZ Pressures for Gas Test 1.....	25
Figure 3-17: Measured and Modelled Test Zone and EDZ Pressures for Gas Test 2.....	26
Figure 3-18: Measured and Modelled Test Zone and EDZ Pressures for Gas Test 3.....	27
Figure 3-19: Sample Gas Saturation Showing Close-up on Test Zone with Gas Pool at the Top .....	28

Figure 3-20: Sample Gas Saturation Outside Test Zone with Red Ring Representing Atmospheric Boundary .....	28
Figure 4-1: T2GGM-FLAC3D Simulator Algorithm .....	30
Figure 4-2: Generalized Mohr-Coulomb Shear Failure Model: (a) Mohr Circle and Mohr-Coulomb Failure Criterion on a Shear Stress- Normal Stress Plot (after Zang and Stephansson 2010); (b) Failure Plane Orientation in Laboratory Tests.....	31
Figure 4-3: UJM Composite Mohr-Coulomb Model Failure Envelope for Intact Rock (After Itasca, 2012).....	32
Figure 4-4: Ubiquitous-Joint Model Composite Mohr-Coulomb Failure Envelope for Bedding Planes (After Itasca 2012).....	33
Figure 4-5: Measured Stress-Permeability Relationships for Single Rock Fractures (Walsh et al. 2008) Compared to HG-A Damaged Zone Stress Permeability Relationship.....	35
Figure 4-6: Test Zone Fluid Pressure Compared to Average Applied Packer Pressure at the Packer-Rock Interface .....	37
Figure 4-7: Permeability Function for the Packer-Rock Interface .....	37
Figure 4-8: Bedding Planes at the Mont Terri URL at a Location Near the HG-A Tunnel .....	38
Figure 4-9: Illustration of Bedding Planes at the HG-A Tunnel (Corkum and Martin 2008) .....	39
Figure 4-10: Cut-away Cross Section Though Model Domain, Comparing FLAC3D and TOUGH2 Geometry .....	40
Figure 4-11: Principle Stresses at the Level of the Mont Terri URL.....	41
Figure 4-12: Initial Pore Pressure Distribution (Shown Here on the T2GGM Model Grid).....	42
Figure 4-13: Illustration of the Two Packer Pressure Application Zones (Applied Force is in Newtons) .....	42
Figure 4-14: Four Failure Modes Delineating the EDZ Extents Compared with a Laser Scan of the Tunnel Wall Following Excavation.....	43
Figure 4-15: Damaged Zone and the Estimated Change in Permeability Compared with the Schematic Representation of the Damaged Zone from Marschall et al. (2006).....	44
Figure 4-16: Estimated Permeability of the EDZ and Its Changes with Time .....	45
Figure 4-17: Estimated Permeability of the Packer-Rock Interface at Four Times .....	46
Figure 4-18: Calculated Water Pressure at the Test Zone Compared with the Measured Pressure .....	47
Figure 4-19: 2D Cross Section of Calculated Water Pressure at Different Times .....	48

## 1. INTRODUCTION

This technical report summarizes the work of Geofirma Engineering between 2011 and 2013 on modelling studies of the HG-A field experiment conducted as part of FORGE (Fate of Repository Gases) Work Package (WP) 4.3 for the Nuclear Waste Management Organization (NWMO). The HG-A field experiment at Mont Terri underground research laboratory (URL) in Switzerland is intended to examine the long-term leakage of water and gas from a small, backfilled and sealed tunnel, identifying the evolution, location, and properties of gas release pathways in a very low permeability host rock (Opalinus clay). This modelling study was divided into two stages. In the first stage, the HG-A was modelled by examining gas and water flow in the Excavation Damage Zone (EDZ) through a two-phase flow model. In the second stage, the flow model was coupled to a geomechanical model to examine the development, extent, and permeability of the EDZ. Of particular interest in all modelling stages was the temporal evolution of permeability in the system (self-sealing) due to swelling of clay, and the effect of hydromechanical coupling (i.e., fluid pressure and confining stress) on the permeability of the EDZ.

For the HG-A experiment, a tunnel approximately 13 m long and 1 m in diameter was excavated in the wall of one of the drifts in the Mont-Terri URL (see Figure 1-1). A series of smaller boreholes were also drilled into the rock surrounding the HG-A tunnel, and instrumented with piezometers and various deformation gauges. Figure 1-2 shows a schematic of the HG-A experimental design, and the locations of the total stress and fluid pressure sensors. The HG-A tunnel itself was divided into three sections. The deepest 4 m of the tunnel (from 9 - 13 m deep) is the test section. It is into this section that water and gas were injected during the experiment, with water injected through a port on the floor of the test section, and gas injected into a port on the roof. The test section was instrumented with piezometers, extensometers, strain gauges, time domain reflectometers (TDRs), and geophones. After the instruments were installed, this section was backfilled with gravel behind a retaining wall. In the next 3 m section of the tunnel, from 6 - 9 m deep, a custom built “megapacker” was installed to seal the tunnel and hydraulically isolate the test section. Water or gas escaping from the test section flow through the EDZ around the packer during the tests. Instruments consisting of piezometers, total stress cells, and TDRs were installed in this section between the packer and the tunnel wall. Following installation of the packer, the volume between the packer and the test-section retaining wall was filled with cement grout. The final 6 m of the tunnel was lined with a steel casing. The gap behind this liner was not grouted or sealed in any way (Lanyon 2011a). There were many more instruments installed which are not shown in Figure 1-2.

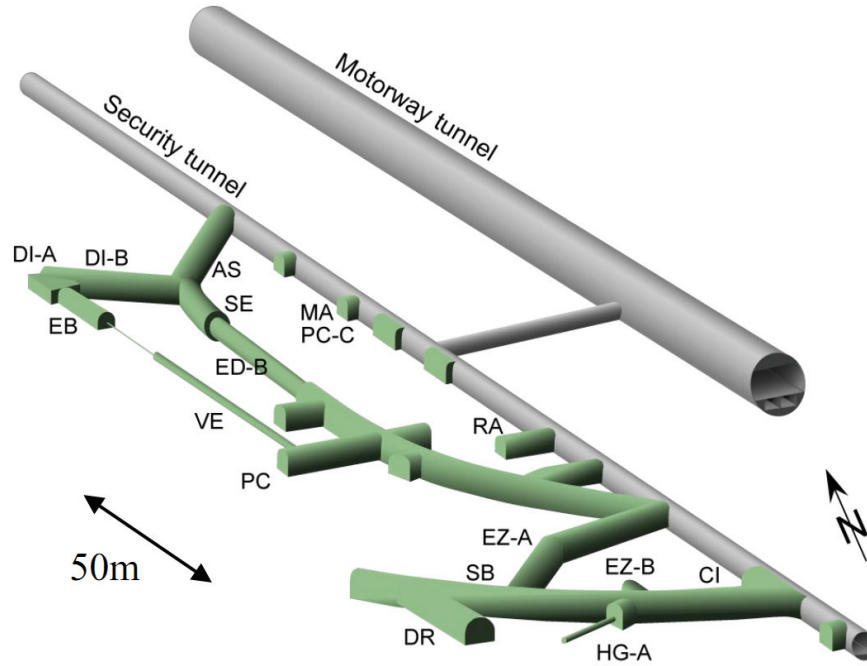
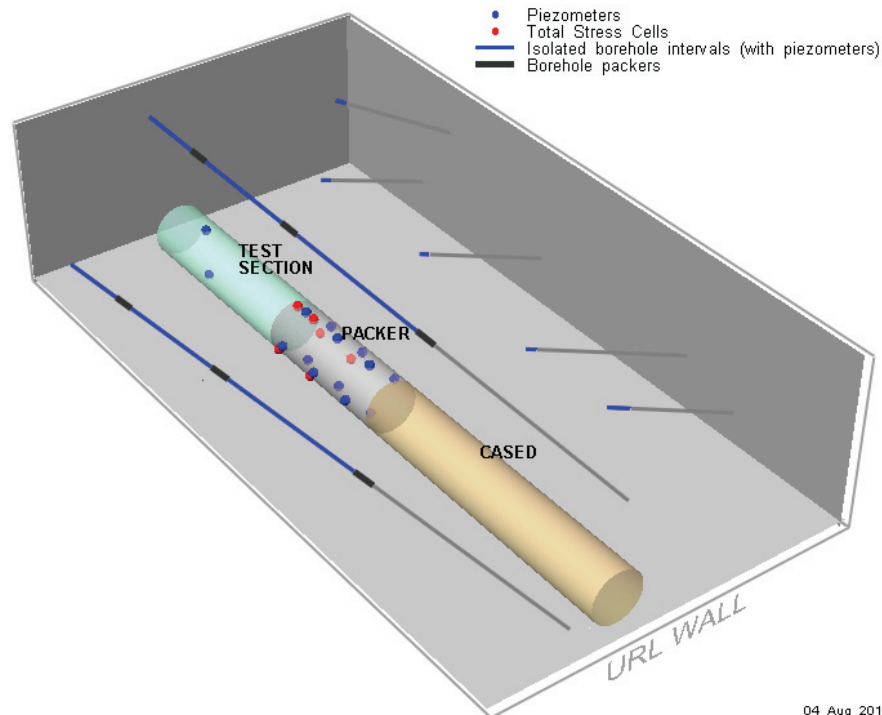


Figure 1-1: Layout of the Mont-Terri URL Showing the HG-A Tunnel at the Bottom Right (from Lanyon et al. 2009)



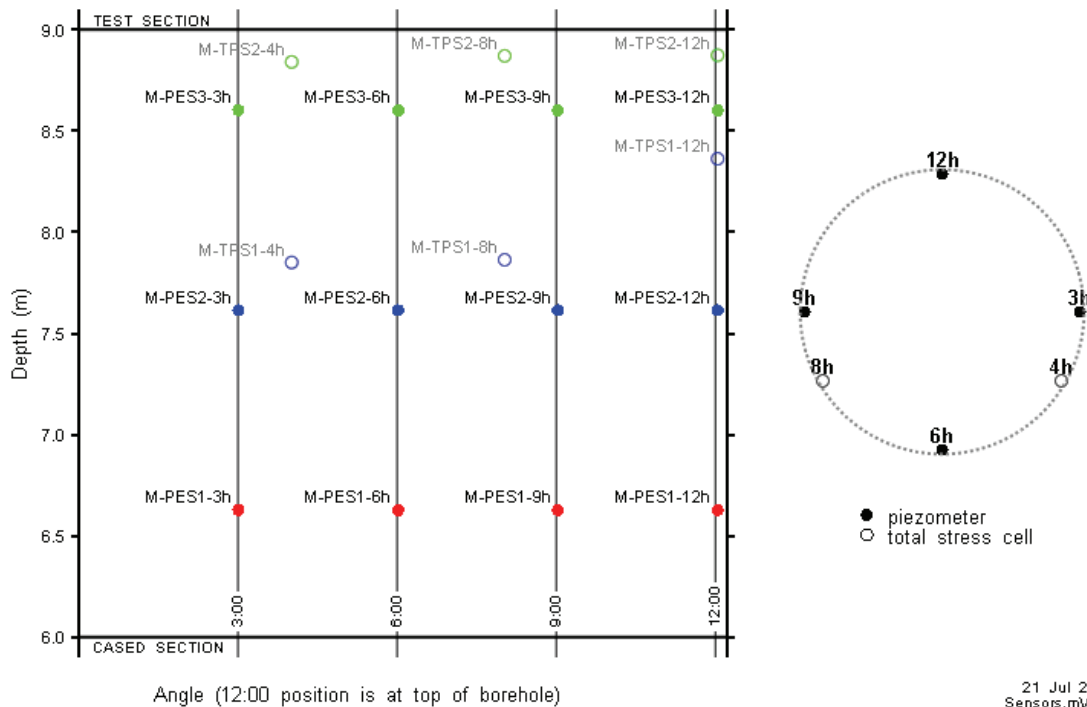
04 Aug 2011  
Sensors.mView

Figure 1-2: Layout of the HG-A Experiment Showing Piezometers and Total Stress Sensors in the HG-A Tunnel and Surrounding Boreholes

## 2. EXPERIMENTAL DATA SET

There is a very large amount of data associated with the HG-A experiment. In implementing and calibrating the models presented in this report, we relied largely on pore pressure and total stress measurements, most of which were measured at the interface between the packer and the tunnel wall. Figure 2-1 shows a 2D projection of the total stress and fluid pressure sensors at the interface between the packer and the tunnel wall, which are useful in interpreting later figures. Figure 2-2 to Figure 2-5 on the following pages summarise some of the data. See Appendix A for sensor locations and description.

The packer was first inflated in November 2006. During 2007 a series of tests in which water was injected into the test section were carried out. The injections were intended to fully saturate the test section, and at the same time test the performance of flow control units and the sensor array (Lanyon et al. 2009). In this phase of the experiment the backfill material was fully saturated by cycling water through the system to dissolve any trapped air, while the EDZ was also resaturated. In January 2008 a multi-rate water injection test was started to investigate sealing phenomena in the EDZ in response to swelling of the claystone, changes in packer pressure (total stress), and changes in pore pressure (causing changes in effective stress). This test continued for 750 days during which the water injection rate and the packer pressure were varied, allowing the examination of how packer pressure influenced the permeability of the EDZ surrounding the packer. Within this report time 0.0 refers to the beginning of the multi-rate water injection test (January 23, 2008 12:00).



Note: Colors correspond to those in Figure 2-2.

**Figure 2-1: 2D Projection of Sensor Locations at the Interface between the Packer and the Tunnel Wall**

Figure 2-2 shows data from the multi-rate water injection test. Shown in the figure are measured pore pressure (pressure of the pore fluid) and total pressure (total mechanical stress) at various locations in the HG-A tunnel, as well as fluid injection rates in the test section. A few points of interest in the data set include:

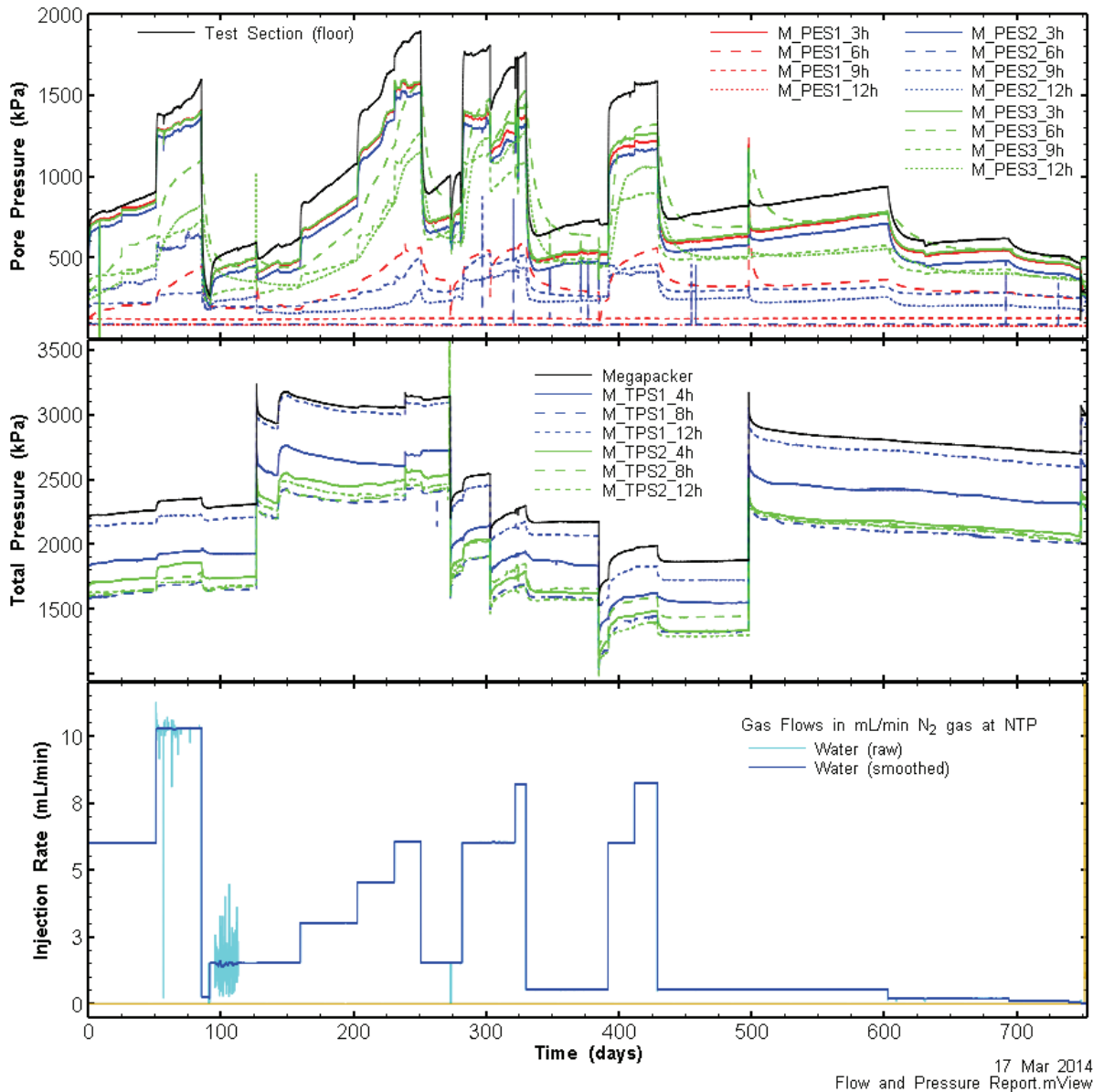
- Generally, higher injection rates led to higher pressures in the test section and along the outside of the packer. However, there was no unique correspondence between injection rate and pressure rise. The highest water injection rate (10 mL/min) occurred between approximately 50 and 85 days, but the maximum pressure was observed at day 250, when the pumping rate was significantly lower (6 mL/min). This is best explained if the permeability of the flow outlet from the system, the EDZ, is not constant. This may be partially explained by the increased packer pressure between days 127 and 273 compressing the EDZ, thereby reducing the permeability.
- For any given change in pumping rate, the pressure in the test zone and beside the packer changed very rapidly, implying a rather low storage coefficient. However, after this rapid equilibration, a gradual, almost linear, pressure rise was observed in almost all cases. This suggests that there was a continuous, gradual reduction in EDZ permeability.
- Large changes in packer pressure are associated with small, sudden changes in test section pore pressure. These sudden pressure changes are very likely caused by small changes in test section volume as the packer expands or contracts, deforming the wall of the test zone.

Figure 2-3 shows a 2D projection of pore pressures at the interface between the packer and the tunnel wall, arranged as shown in Figure 2-1. This presentation of the data makes clear what was not obvious in Figure 2-2: there is evidence of a high permeability channel at roughly the 3 o'clock position on the tunnel wall. All sensors at the 3 o'clock position showed large and rapid responses to pressure in the test zone; however, the lack of a pressure gradient along the channel suggests that this channel is not well connected to the atmospheric boundary (Lanyon, 2012). In other words, the channel is blocked somewhere downstream of the M-PES-1 plane (near the cased zone). There was also a smaller response to changes in test zone pressure between 9 and 12 o'clock with a roughly linear pressure gradient, indicating the existence of a second permeable channel, this time connected to the atmospheric boundary. The majority of flow must be following a preferential flow pathway (or pathways) near the 9 o'clock location. The existence of these channels is consistent with qualitative observations of the damage zone surrounding the tunnel (see Figure 2-4).

Figure 2-5 shows data from the three gas injection tests. The figure displays measured pore pressure (pressure of the pore fluid) and total pressure (total mechanical stress) at various locations in the HG-A tunnel, as well as fluid injection rates in the test section. A few points of interest include:

- There is clear evidence for breakthrough of gas in tests Gas Test 2 and Gas Test 3. In both tests there is a clear inflection point after which gas pressure decays. This occurs without any changes in the pumping rate, and is presumably caused by the development of a continuous gas filled pathway connecting to the atmosphere.
- Pressures were kept high and relatively stable during the gas injection tests, with a gradual decay of total pressure with time.
- In Gas Test 2 and Gas Test 3, there are additional inflection points on the pressure curve. For instance, around day 1267 in Gas Test 3 the pumping rate dropped for 2 days. When

pumping resumed at the same rate, pressure rose to a new equilibrium. This may have been due to collapse of an unstable gas flow pathway when the injection rate dropped.



Note: Time = 0.0 is January 23, 2008 at 12:00. Colors in pore and total pressure curves correspond to those in Figure 2-1.

**Figure 2-2: Multi-rate Hydraulic Test Data from the HG-A Experiment**

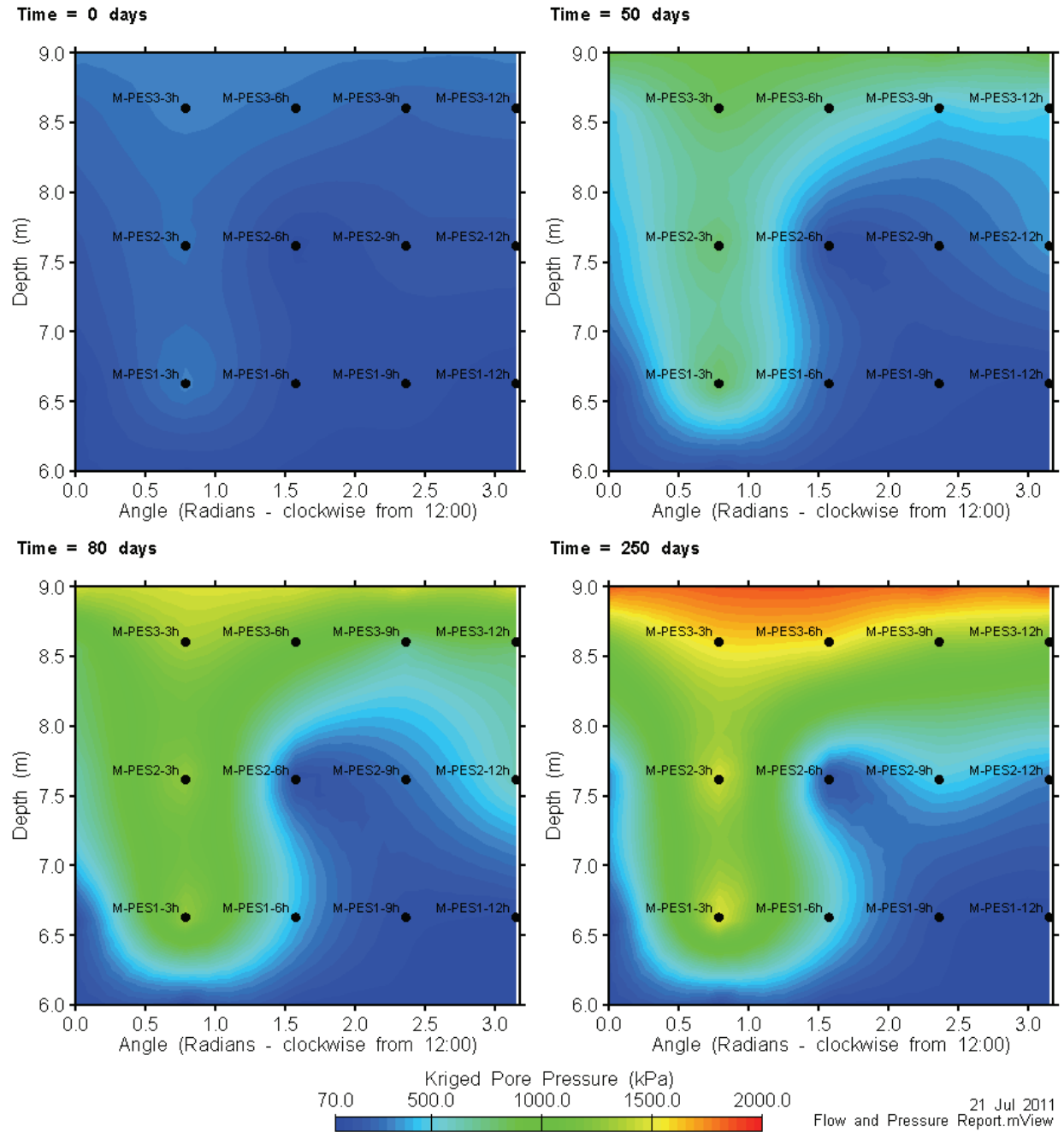


**Figure 2-3: 2D Projection of Pore Pressures at the Interface between the Packer and the Tunnel Wall**

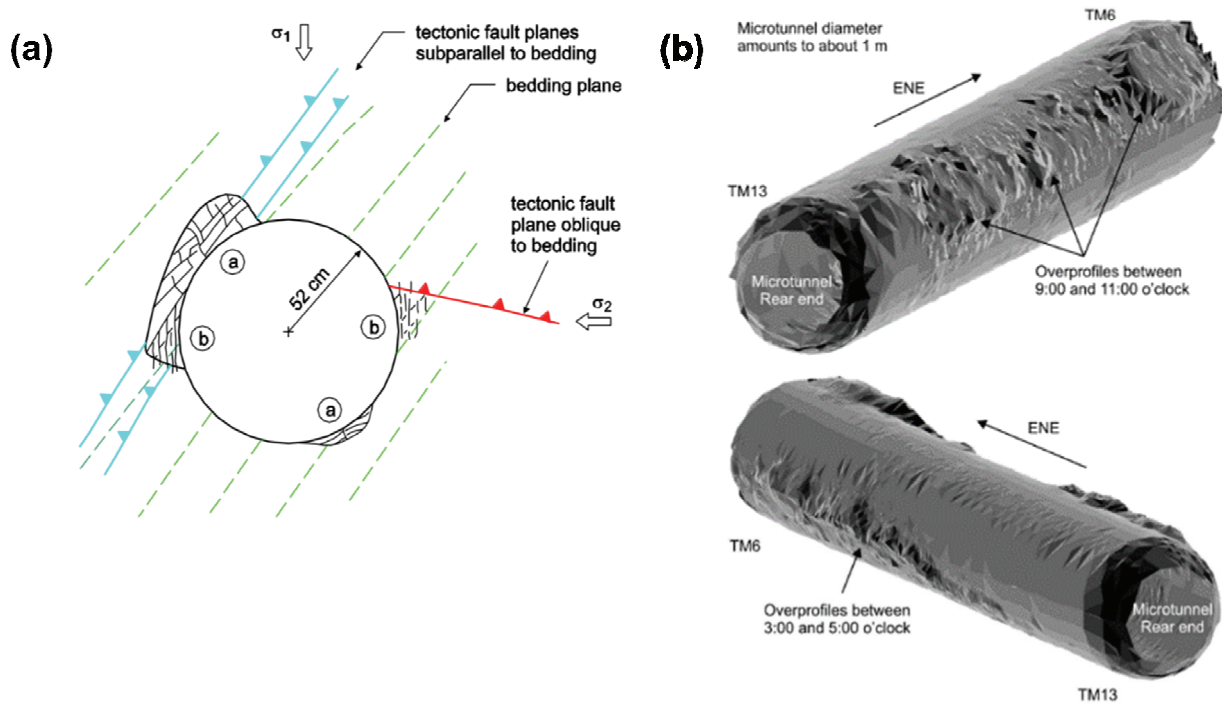
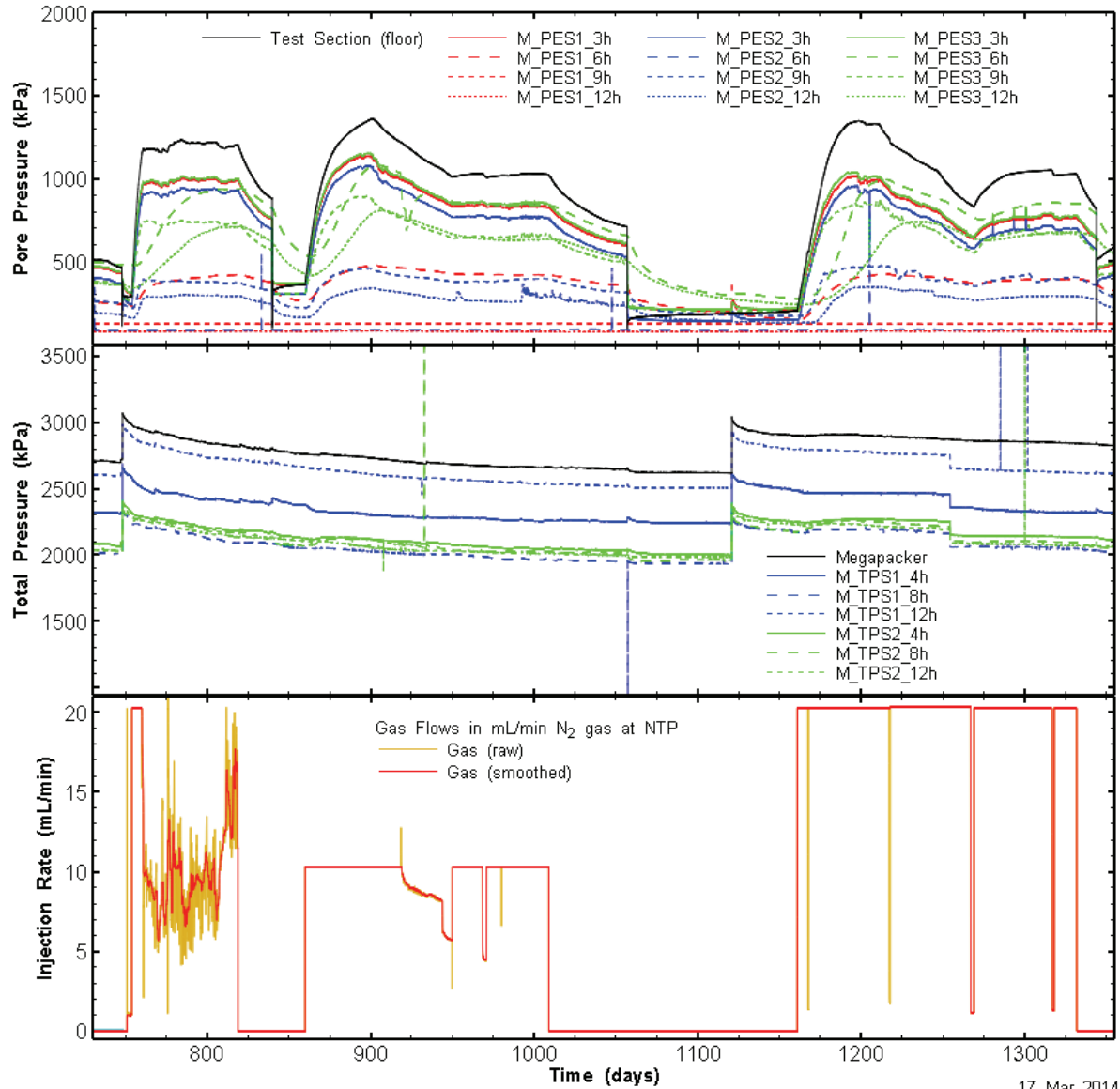


**Figure 2-4: Damage Zone around Tunnel (a) Schematic Representation and (b) Laser Scans of the Tunnel between 6 and 13 m Depth (from Marschall et al. 2006)**



17 Mar 2014  
Flow and Pressure Report.mView

Note: Time = 0.0 is January 23, 2008 at 12:00. Colors in pore and total pressure curves correspond to those in Figure 2-1.

**Figure 2-5: Gas Injection Test Data from the HG-A Experiment**

### 3. TWO-PHASE FLOW MODELLING

Two phase flow modelling employed two models, described as follows:

- 1) 2D Hydraulic Model: The HG-A experiment clearly lends itself to modelling with a radial grid. We did initial modelling work with a 2D radial grid, assuming that the problem and property distribution is approximately axisymmetric.
- 2) 3D Hydraulic Model: 3D radial grid of the system which incorporated the effect of gas buoyancy and the apparent heterogeneous permeability of the EDZ (e.g. Figure 2-3).

Currently the models are split into four stages, encompassing the water-only Multi-rate Flow Test from days 0 to 750 (referred to as Water Flow), and three gas tests, which cover days 753 to 840 (Gas Test 1), 859 to 1057 (Gas Test 2), and 1160 to 1345 (Gas Test 3). The three gas tests were separated because before each test there was a gas/water exchange cycle which required the pressure and saturation in the test zone to be reset.

#### 3.1 CODE USED

For the 2D and 3D hydraulic model, the current Geofirma version of TOUGH2 was used (T2GGM\_GF\_V3.1). T2GGM is a code that couples TOUGH2 with the Gas Generation Model, GGM (Suckling et al. 2012). The gas generation capabilities of T2GGM were not used for this project. TOUGH2 is a general-purpose numerical simulation program for multi-phase fluid and heat flow in porous and fractured media developed by Lawrence Berkeley National Laboratory (Pruess et al. 1999). The EOS3 equation of state module used in T2GGM simulates the transport of a single separate ideal gas phase in water (note that T2GGM allows for specification of alternate gases to air, the EOS3 default). EOS3 also models the transport of dissolved gas in water by diffusion and advection. Dispersive processes are not modelled.

For HG-A modelling, pure nitrogen is modelled instead of air. To facilitate HG-A modelling, a new function allowing the specification of time-dependent permeability was implemented in T2GGM. This function allows the user to select a subset of nodes in the model domain and specify a tabular time dependent multiplier modifying the assigned permeability at these nodes.

#### 3.2 MODEL SETUP

##### 3.2.1 2D Radial Hydraulic Model

Initial modelling of the HG-A experiment used a 2D radial model to represent the HG-A experimental geometry. The radial model does not take into account the clear evidence of preferential flow pathways in the tunnel EDZ. However, for the purposes of simulating the pressure transients in the test section during the multi-rate flow test, and thereby estimating the bulk transmissivity of the EDZ around the packer, a radial model is sufficient and much faster than a 3D model of the system. The radial grid is a 2D representation of the full 3D system. The volumes of the 2D blocks making up the model are equal to the volume the block would have if the 2D grid were rotated a full 360 degrees about the Y-axis. The grid, shown in Figure 3-1, has 1172 nodes (blocks) and 2263 connections. The model is 14 m long, extending from the tunnel wall to approximately 1 m beyond the end of the HG-A tunnel. The 3 m model radius extends from the centre of the HG-A tunnel to 2.5 m into the surrounding rock beyond the wall of the tunnel.

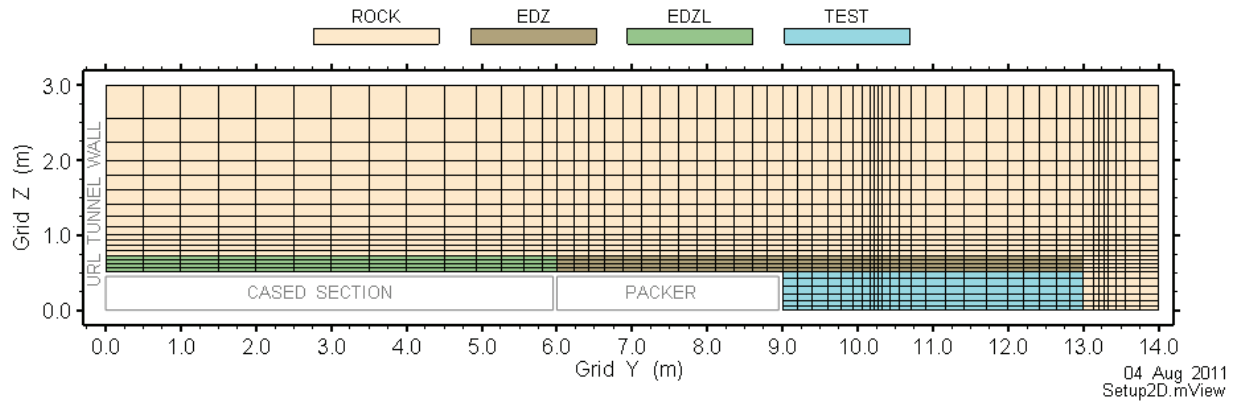


**Figure 3-1: 2D-Radial Grid Discretization**

As shown in Figure 3-1, the 2D radial model was divided into 4 property groups:

- 1) ROCK – representing the intact Opalinus clay formation surrounding the tunnel.
- 2) EDZ – representing the EDZ surrounding the test section and the packer. Based on initial characterization work (see Figure 2-4), the EDZ was presumed to have a thickness of 20 cm. This is the same assumption made by Lanyon et al. (2009) in their initial modelling work. The tunnel in the packer section of the borehole was smoothed using a synthetic resin for a tight seal between the tunnel wall and the packer.
- 3) EDZL – representing the EDZ behind the steel casing in the first 6 m of the tunnel. This zone is modelled with higher permeability than the other EDZ zone. There was no cement or grout injected behind the casing so this is likely to be very permeable (Lanyon, 2011a).
- 4) TEST – representing the gravel-filled test zone at the end of the HG-A tunnel.

Model properties are shown in Table 3-1. The permeability of the EDZ parameter is not shown in the table as it was not modelled as stationary parameter in most of the models. Initial estimates of parameter values were based on Lanyon et al. (2009) or on model calibration against the water injection test results. The chosen calibration target (i.e., the test zone pressure) was not very sensitive to most parameters. Important parameters are EDZ permeability and test zone compressibility.

**Table 3-1: Model Properties for Water Saturated Flow**

Material	Porosity (-)	Permeability <sup>A</sup> (m <sup>2</sup> )	Pore Compressibility (Pa <sup>-1</sup> )
ROCK	0.1370 <sup>C</sup>	1.12E-20 <sup>C</sup>	6.44E-11 <sup>E</sup>
EDZ	0.2055 <sup>D</sup>	<i>variable</i> <sup>B</sup>	2.96E-10 <sup>E</sup>
EDZL	0.2055 <sup>D</sup>	1.23E-14 <sup>F</sup>	2.96E-10 <sup>E</sup>
TEST	0.3500 <sup>F</sup>	1.12E-14 <sup>F</sup>	2.20E-10 <sup>G</sup>

<sup>A</sup> Assumed isotropic.

<sup>B</sup> Time-varying, values range from approximately 1E-16 to 1E-15 m<sup>2</sup>, based on model calibration.

<sup>C</sup> Source: Lanyon et al. (2009).

<sup>D</sup> Intact rock porosity multiplied by 1.5.

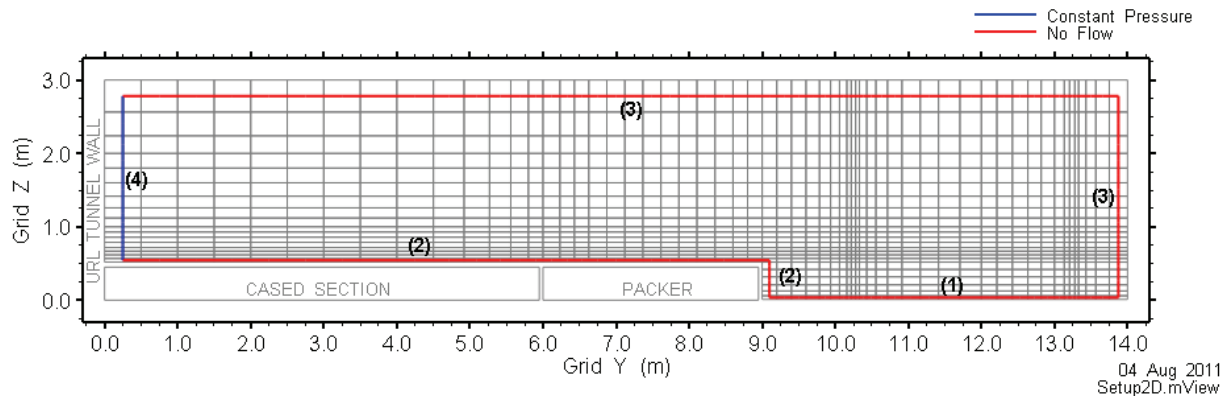
<sup>E</sup> Based on model calibration.

<sup>F</sup> Estimated.

<sup>G</sup> Estimated in a limited calibration exercise, not described in the report.

### 3.2.1.1 Boundary Conditions

The 2D radial model boundary conditions are as follows: The top, bottom and right boundaries are no-flow boundaries, while the left boundary (toward the HG-A access tunnel) is a constant pressure boundary set to 101.3 kPa (1 atm). Boundary conditions are shown in Figure 3-2.



Note: Boundary conditions are based on (1) symmetry, (2) adjacency to impermeable casing or packer, (3) assumption that flow across the boundary is negligible, and (4) boundary is exposed to the atmosphere.

**Figure 3-2: 2D-Radial Model Boundary Conditions**

### 3.2.1.2 Initial Conditions

The initial pressure distribution for the Water Flow Model is shown in Figure 3-3, and is largely based on extrapolation from measured data. The initial pressure in the test zone was set to 330 kPa. In the EDZ, the initial pressure distribution is a linear decline from 330 kPa (the measured test zone fluid pressure at time = 0.0 days; see Figure 2-5) in the test zone to 101.3 kPa at the left boundary. Based on available measurements (see Figure 3-4), the initial pressure in the intact rock was also made a linear function, declining from 530 kPa at the right boundary to 101.3 kPa on the left boundary (URL side). This is a rough approximation of the more complex pressure distribution evident in Figure 3-4. The initial water saturation in the host

rock was set to 1.0 throughout the model domain, and remained there for the entire model run. The temperature was set to 13 °C, and the model was run isothermally (i.e., no temperature change was modelled).

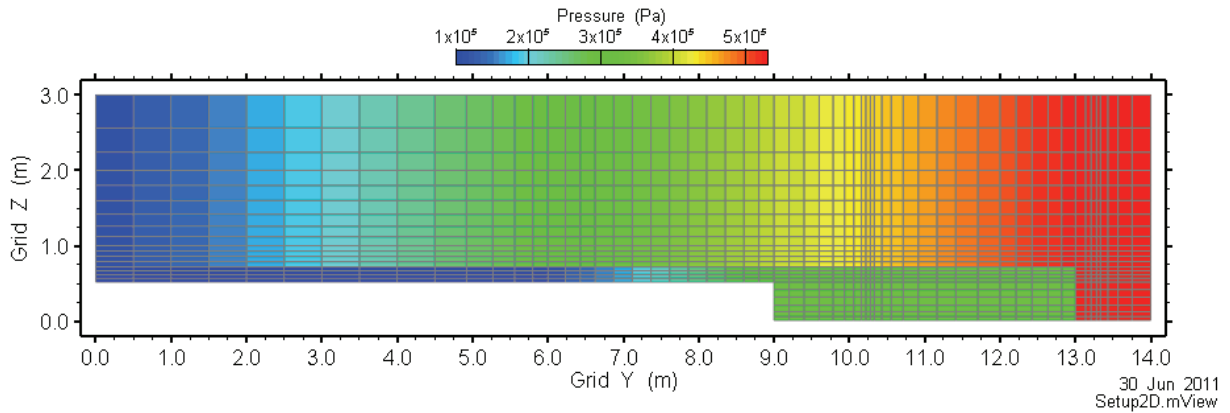


**Figure 3-3: 2D-Radial Model Initial Pressure Distribution for the Water Flow Model**

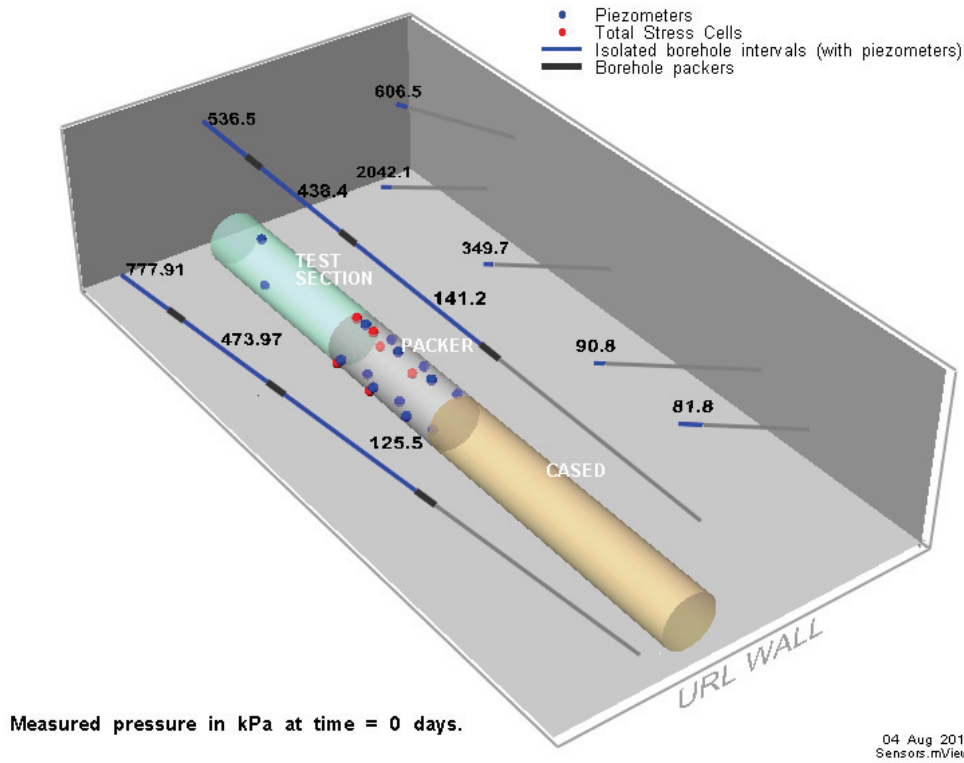


**Figure 3-4: Measured Formation Pore Pressures at Time = 0.0 days (Lanyon 2011b)**

### 3.2.1.3 Source Term

During the course of the experiment, water was continuously injected into the test zone, at varying rates. As there were oscillations in some parts of the flow curve, injection was modelled using a simplified version of this curve as a source term. The source term for the Water Flow Model is shown in Figure 3-5.

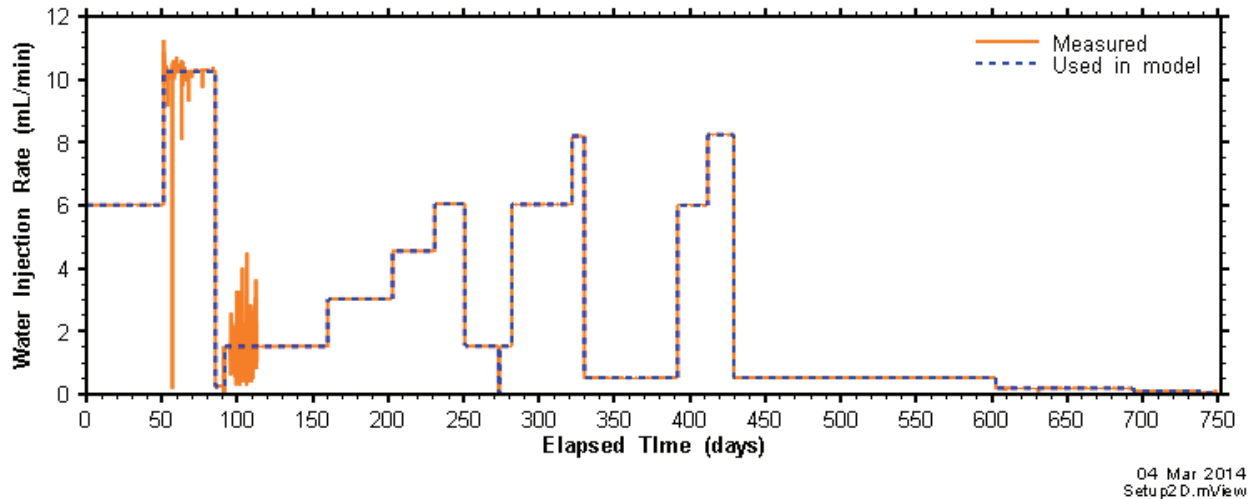


**Figure 3-5: Measured Injection Rates and Flow Rates Used in the Water Flow Model**

### 3.2.1.4 Time Varying Permeability

The first model runs used constant values for the EDZ permeability. However, this approach was found to be inadequate (see Section 3.3.1.1), not accounting for the apparent effect of swelling of Opalinus clay in contact with water and hydromechanical coupling in the EDZ due to changes in effective stress. TOUGH2 does not have the ability to calculate the impact of swelling on fracture permeability, nor does it have a hydromechanical coupling capability. To bypass this limitation, a new subroutine allowing the specification of time-dependent permeability was implemented in T2GGM, allowing selection of a subset of the model domain and specification of a time-dependent permeability multiplier function in that sub-domain.

To develop the time dependent permeability function itself, the rate of water injection and the resulting change in pressure was used. For this analysis, the test section was idealised as a closed volume with one inlet (the water injection valve) and one outlet (the EDZ). It was further assumed that the response in any given time step could be modelled as steady-state flow. This second assumption is supported by the very rapid equilibration of the system to changes in pumping rate, as seen in the test section pressure curve (Figure 2-2). Constant water density was also assumed. With these assumptions, it was possible to solve for the apparent permeability of the EDZ ( $k_{EDZ}$ ) using the following expressions:

$$Q_{out} = Q_{in} - \frac{CV_{test}dP}{dt} \quad (1)$$

$$k_{EDZ} = \frac{Q_{out}\mu L}{\Delta P A} \quad (2)$$

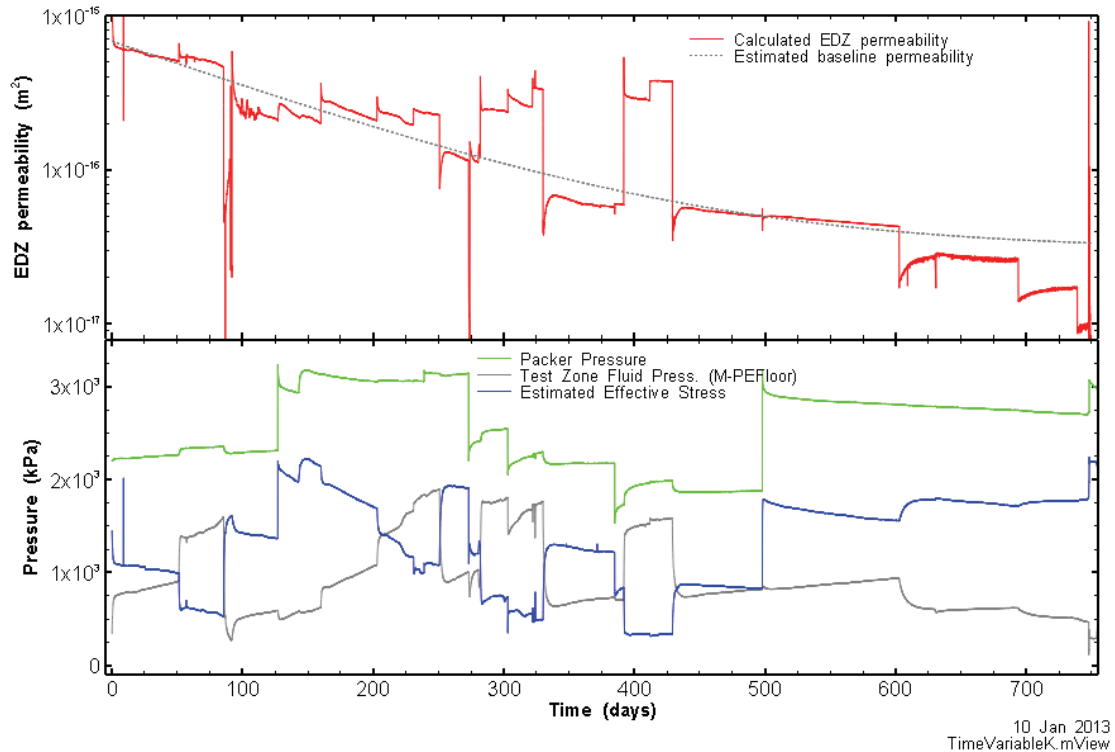
Where:

- $Q_{out}$  = the water outflow rate (function of EDZ permeability), ( $\text{m}^3 \cdot \text{s}^{-1}$ );
- $Q_{in}$  = the water injection rate (measured), ( $\text{m}^3 \cdot \text{s}^{-1}$ );
- $C$  = the bulk test zone compressibility ( $C_{test\ zone} + n * C_{water}$ ), ( $\text{Pa}^{-1}$ );
- $C_{test\ zone}$  = the test zone compressibility ( $\text{Pa}^{-1}$ );
- $C_{water}$  = the water compressibility ( $\text{Pa}^{-1}$ );
- $n$  = the porosity (unitless);
- $V_{test}$  = the approximate test zone volume ( $\text{m}^3$ );
- $dP$  = the pressure change during time step (Pa);
- $dt$  = the time step length (s);
- $\mu$  = the fluid viscosity ( $\text{Pa} \cdot \text{s}$ );
- $L$  = the length over which pressure-loss  $\Delta P$  occurs, assumed to equal the length of the packer (m);
- $\Delta P$  = the pressure drop along length L (Pa); and
- $A$  = the cross sectional area of the EDZ, assumed to be a uniform 20 cm thick ring around the microtunnel ( $\text{m}^2$ ).

Equations (1) and (2) embody what is essentially a very simplified analytical model of the experimental system. The resultant variable permeability curve for the Water Flow Model is shown in Figure 3-6. Over the course of 750 days, this calculation yields an overall permeability drop that is slightly less than two orders of magnitude. Even after this drop, the EDZ permeability remains 3 orders of magnitude higher than the estimated permeability of intact Opalinus clay. This overall decline of EDZ permeability has been observed in works by other authors (e.g., Lanyon et al. 2009, Bernier et al. 2007), and is thought to be caused by healing of fractures due to ongoing swelling of the Opalinus clay in the EDZ. This gradual drop is punctuated by sudden permeability increases that are largely correlated with reduced effective stress in the EDZ adjacent to the packer. The estimated average effective stress (packer total pressure minus test zone fluid pressure) at the 3 o'clock position in the packer-adjacent EDZ is also shown in Figure 3-6. As shown in the figure, EDZ permeability (and potentially the interface permeability) increases are particularly high when packer pressure is low and test zone pressure is high, a hydromechanical effect. The superposition of gradual self-sealing and hydromechanical coupling is what leads to the EDZ permeability curve in Figure 3-6. The "Estimated baseline permeability" curve in Figure 3-6 is an exponential decay function describing a qualitative estimate of what the EDZ permeability function would look like if hydromechanical coupling were not occurring. The rate of permeability decay due to self-healing is very similar to that reported for laboratory-scale samples in Bernier et al. (2007). The "Estimated baseline permeability" curve was not used in modelling, and is provided for illustrative purposes. Instead, the "Calculated EDZ permeability" was used in modelling.

There are a few processes complicating the interpretation of the EDZ permeability. At 127 days the packer pressure was increased by roughly 900 kPa, while at the same time there was a small pressure drop in the test zone fluid pressure. Using Equations (1) and (2), this is interpreted as a small rise in permeability, allowing more water to escape from the test zone. This seems to contradict the idea that increasing the effective stress will reduce the permeability. However, what actually happened at this time was a slight increase in test zone volume (approximately ~35 mL) due to the increased packer pressure pushing on the tunnel walls. All other changes in packer pressure have similar minor effects on the apparent

permeability of the EDZ, but this does not invalidate the overall interpretation of the presence of and causes of permeability changes in the tunnel EDZ.

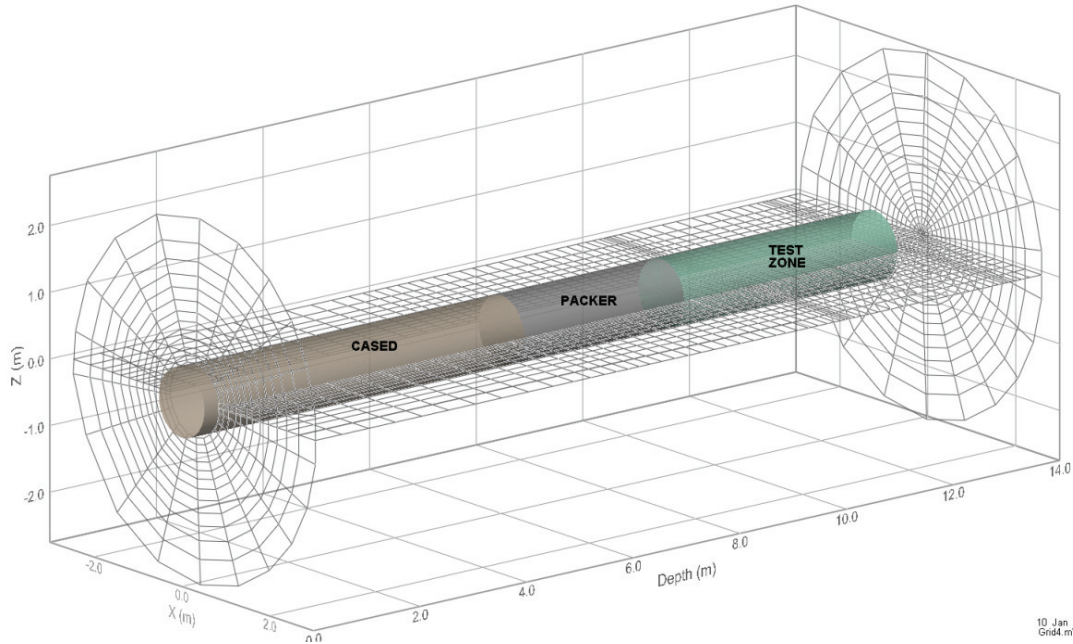


Note: EDZ permeability was calculated using Equations (1) and (2).

**Figure 3-6: EDZ Permeability for Water Flow, and Pressure Data Used for Interpretation of the EDZ Permeability**

### 3.2.2 3D Radial Hydraulic Model

In order to more accurately model the gas injection tests, including features such as gas buoyancy and a preferential gas flow path, a 3D radial model of the HG-A experiment was developed. The grid, shown in Figure 3-7, has 18211 nodes (blocks) and 53670 connections and covers the same volume as the 2D radial grid.



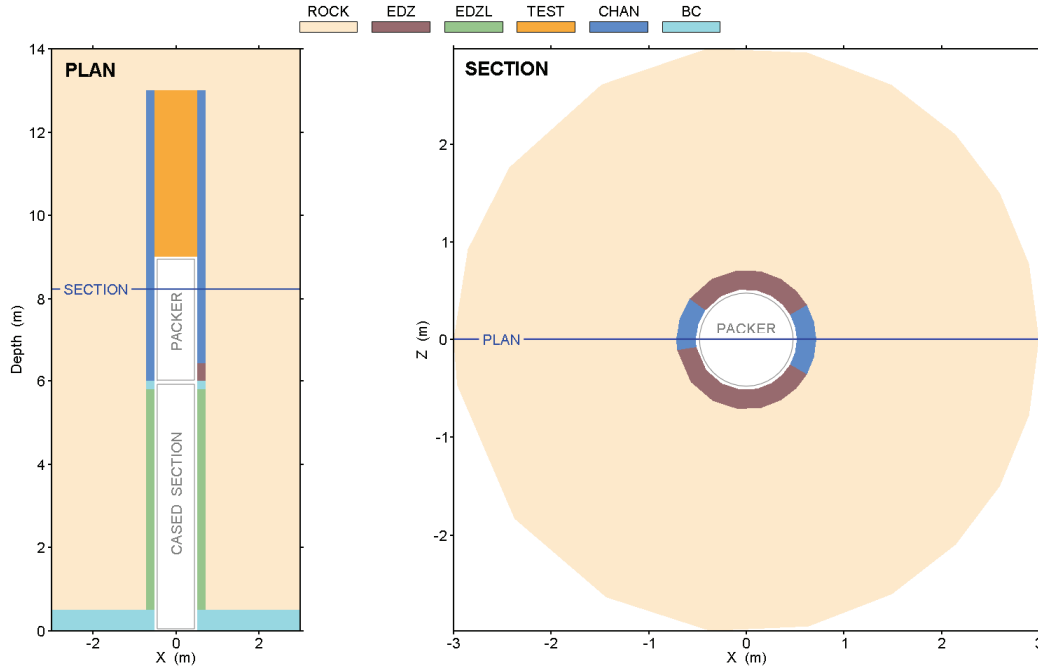
Note: Two cross sections and one plan section of the grid and locations of three tunnel areas are shown.

**Figure 3-7: 3-D Model Discretization**

### 3.2.2.1 Properties

The property distribution of the 3D model shown in Figure 3-8 is similar to the 2D model; however in the EDZ there are high permeability channels at the 3 and 9 o'clock position to reflect what is believed to be a high permeability channels at these locations (see Section 2). As discussed in Section 2, the channel at 3 o'clock is believed to be disconnected from the boundary.

The model properties for the 3D modelling are presented in Table 3-2. They are largely the same as those in Table 3-1, except that EDZ permeability was reduced and the new permeable EDZ channel permeability is approximately 6 times higher than the calculated permeability from the 2-D radial model (see Figure 3-8), thereby maintaining the same overall transmissivity of the EDZ. The channel permeability during the gas injection tests was not time-variant as in the hydraulic tests, except for Gas Test 3, which modified the channel permeability over time to simulate unstable gas pathways.



Note: The property labelled CHAN represents a higher permeability channel. The packer and casing locations are shown for illustration, flows cannot cross these boundaries.

**Figure 3-8: 3-D Model Property Distribution**

**Table 3-2: Model Properties for Gas Injection Tests**

Material	Porosity (-)	Permeability <sup>A</sup> (m <sup>2</sup> )	Pore Compressibility (Pa <sup>-1</sup> )
ROCK	0.137 <sup>C</sup>	1.1E-20 <sup>C</sup>	6.4E-11 <sup>E</sup>
EDZ	0.206 <sup>D</sup>	1.0E-18 (Hydraulic) 1.2E-17 (Gas Test 1) <sup>E</sup> 1.1E-18 (Gas Test 2) <sup>E</sup> 1.1E-18 (Gas Test 3) <sup>E</sup>	3.0E-10 <sup>E</sup>
EDZL	0.206 <sup>D</sup>	1.2E-14 <sup>F</sup>	3.0E-10 <sup>E</sup>
TEST	0.300 <sup>F</sup>	1.1E-14 <sup>F</sup>	2.2E-10 (Hydraulic) 1.2E-08 (Gas Tests 1 & 2) <sup>E</sup> 3.5E-08 (Gas Test 3) <sup>E</sup>
CHAN	0.100 <sup>E</sup>	variable (Hydraulic) <sup>G</sup> 2.0E-16 (Gas Test 1) <sup>E</sup> 2.9E-16 (Gas Test 2) <sup>E</sup> variable (Gas Test 3) <sup>B</sup>	3.0E-10 <sup>E</sup>

<sup>A</sup> Assumed isotropic.

<sup>B</sup> Base value of 3.05E-16 m<sup>2</sup> with time-varying scaling factors applied. Time-variant values range from 5.0E-16 to 2.1E-16 m<sup>2</sup>.

<sup>C</sup> Source: Lanyon et al. (2009).

<sup>D</sup> Intact rock porosity multiplied by 1.5.

<sup>E</sup> Based on model calibration using the pressure results from the gas injection tests.

<sup>F</sup> Estimated.

<sup>G</sup> See Section 3.2.1.4. Combined channel and EDZ permeability is approximately 6 times higher than the EDZ permeability from the 2-D radial model.

Modelling of the gas tests required an increase in test zone pore compressibility in comparison to the hydraulic test analysis, likely due to the presence of small volumes of free gas in trapped the test zone. The properties for the gas injection tests also required minor changes between each gas injection test. Gas Test 1 required changes to EDZ and channel permeability, and Gas Test 3 required a further increase of test zone compressibility and a time varying channel permeability. Possible reasons for these changes between different model runs are discussed in later sections.

The decrease in EDZ permeability between Gas Test 1 and 2 is likely a relative permeability decrease for water, rather than an absolute decrease in permeability, caused by the presence of gas in the EDZ. The increase in test zone compressibility required for Gas Test 3 suggests that flushing of the test zone was incomplete, and some gas remained in the test zone at the start of the test. The required time varying permeability indicates the existence of unstable gas flow pathways through the EDZ.

Table 3-3 shows model properties specific to two-phase flow modelling (i.e., van Genuchten parameters). See Appendix B for van Genuchten model and parameters. The values in Table 3-3 are not specific to the Opalinus clay, but rather represent a set of generic parameters for low permeability rock that are within the reasonable range for Opalinus clay identified in Marschall et al. (2005). In the test zone, the model currently assumes that the capillary pressure is zero, and that the relative permeability is a linear function of the liquid saturation. Capillary pressure and relative permeability curves based on Table 3-3 are shown in Figure 3-9.

**Table 3-3: Model Properties for Two-Phase Flow (van Genuchten Properties)**

Material	n	m	$1/\alpha$ (Pa)	$S_{lr}$	$S_{gr}$
ROCK	1.75	1	12.0E+06	0.25	0.05
EDZ	1.75	1	3.0E+06	0.25	0.05
EDZL	1.75	1	3.0E+06	0.25	0.05
CHAN	1.75	1	2.0E+06	0.25	0.00
TEST <sup>A</sup>				0.01	0.01

<sup>A</sup> Relative permeability is a linear function from 0 to 1 between residual saturations.

The increased permeability in the channel is believed to be due to the presence of significant and connected fractures. In effect, this makes the channel EDZ a dual-porosity system in which the capillary pressure in the fractures would be significantly lower than that in the EDZ matrix (Zhang and Fredlund 2003). In order to account for this, an adjustment was made to the capillary pressure curve for the channel material. We assumed that capillary pressure in the fractures would be equal to zero, and therefore modified the capillary pressure curve to equal zero below a certain gas saturation, which can be considered to equal the fracture pore volume ratio. Through model calibration, a modified capillary pressure curve where capillary pressure is zero for water saturations above 0.985 was found to be generally optimal. Based on our conceptualization, this is equivalent to saying that the major permeable fractures were found to comprise approximately 1.5 percent of the total pore volume. When gas saturation moves beyond 1.5%, the model calculates the capillary pressure using the van Genuchten equations and the parameters in Table 3-3.

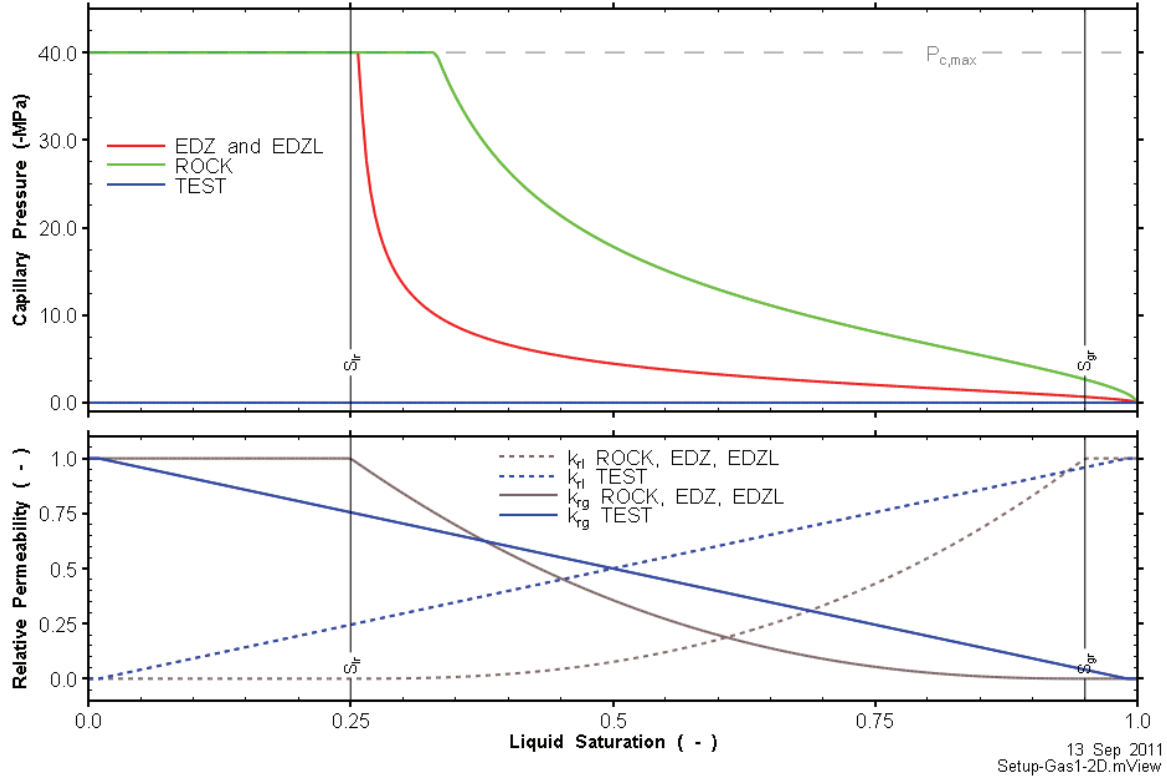
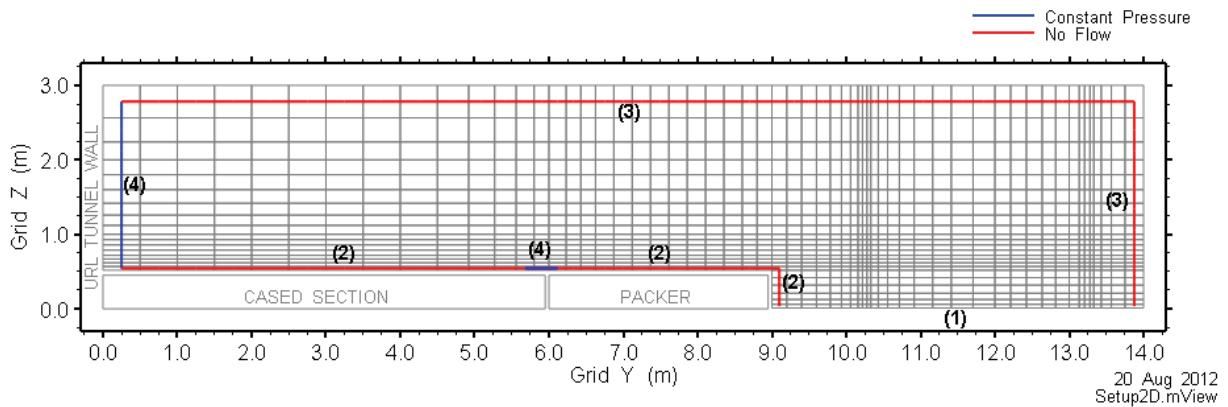


Figure 3-9: Capillary Pressure and Relative Permeability Curves

### 3.2.2.2 Boundary Conditions

Boundary conditions for the 3D model shown in Figure 3-10 are the same as the 2D model except for the addition of an atmospheric boundary at the interface between the liner and the packer. Since the lined section of the microtunnel is unsealed, and there is an open surface between the liner and packer (Lanyon 2011a), an atmospheric boundary condition is a reasonable assumption.



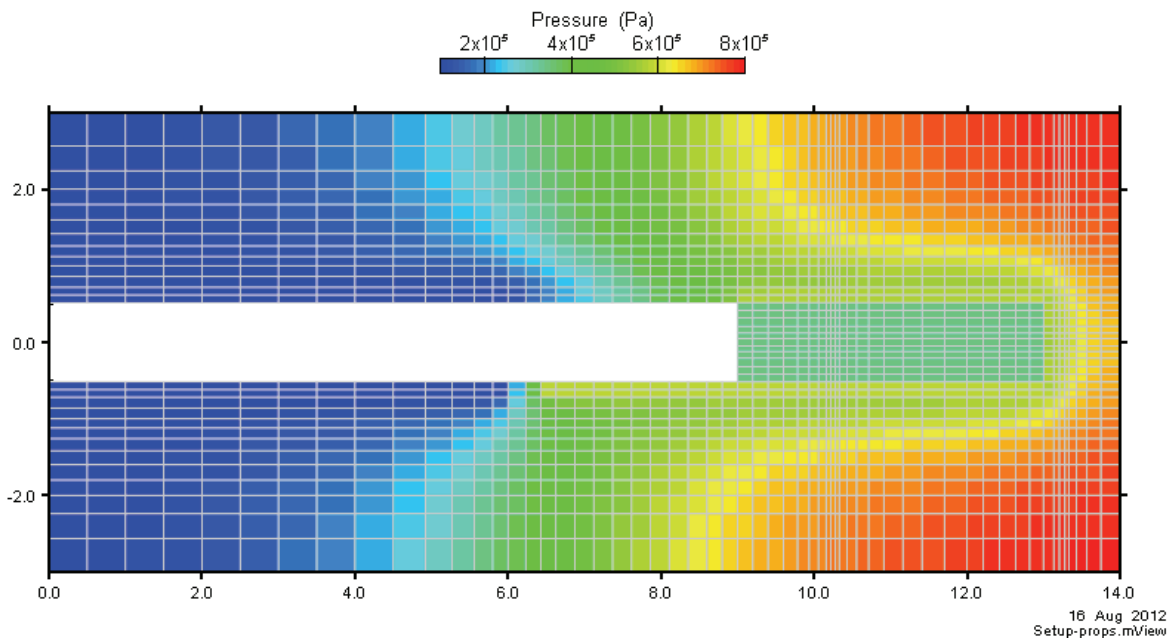
Note: Boundary conditions are based on (1) symmetry, (2) adjacency to impermeable casing or packer, (3) assumption that flow across the boundary is negligible, and (4) boundary is exposed to the atmosphere.

Figure 3-10: 3D-Radial Model Boundary Conditions

### 3.2.2.3 Initial Conditions

The initial pressure distribution for the Water Flow Model was set exactly the same as the initial conditions for the 2D model. For the gas injection tests, the initial pressure was based on the final pressure distribution of the previous test.

Before each gas injection test, there were gas/water exchanges. The test section was depressurised, water was cycled through the test section, and water leaving the test zone was degassed in equilibrium with atmospheric pressure. After the gas/water exchanges the test section was closed off again (Lanyon 2011b). Therefore, for the Gas Flow Model the initial pressure in the test section was set to the observed pressure at that time. An example of an initial pressure distribution for the Gas Flow Model is shown in Figure 3-11.



**Figure 3-11: 3D-Radial Model Typical Initial Pressure Distribution for the Gas Flow Model (Plan Section View)**

### 3.2.2.4 Source Term

The source term used for the multi-rate hydraulic test was the same as for the 2D model described in Section 3.2.1.3. The source term for the gas injection tests is shown in Figure 3-12. This curve largely follows the experimental curve but the extreme oscillations in gas injection rates during Gas Test 1 were smoothed to improve numerical stability of the model. During the gas injection, there was also a continuous injection of water at a low rate of 0.02 mL/min.

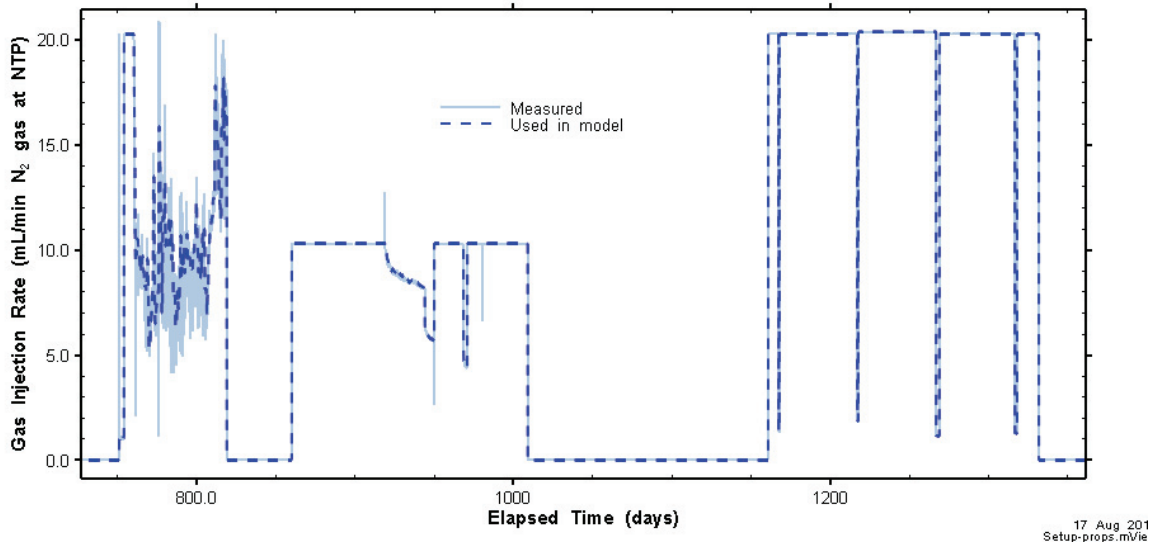


**Figure 3-12: Measured Injection Rates and Flow Rates Used in the Gas Flow Models**

### 3.3 RESULTS AND DISCUSSION FOR 2D AND 3D MODELS

#### 3.3.1 2D Model Results

For the 2D models, the comparison between measured and modelled pressures focuses on the test zone pressure, which is largely a function of the EDZ transmissibility. The 2D radial model cannot accurately reflect the pressure distribution along the packer wall as it cannot include EDZ heterogeneity. The 3D modeling of the HG-A experiment is presented in section 3.3.2.

##### 3.3.1.1 Water Flow Model: Constant EDZ Permeability

Results for the 2D radial model of the water-only multi-rate flow test with constant EDZ permeability are presented in this section. Figure 3-13 shows test zone pressures for three different models. The material properties in these models are the same as those in Table 3-1, with the permeability of material group EDZ (see Figure 3-1) changed between models. Three different EDZ permeabilities were used:  $2.5 \times 10^{-16} \text{ m}^2$ ,  $5.0 \times 10^{-16} \text{ m}^2$ , and  $1.0 \times 10^{-15} \text{ m}^2$ . There are a number of notable results. Firstly, it is clear that none of these models match the measured pressures in the test zone. All models under-predict pressures at some times and over-predict at other times. The various models come close to the measurement at some times, but there is no consistently good match. Although the set of models brackets the actual behaviour at most pressures, beyond 250 days all models consistently under-predict pressure during the pressure minima which occur when fluid injection rates are low (see rates in Figure 2-2), suggesting that the actual EDZ permeability should be lower than all models. However, at high injection rates this no longer holds true. Taken together, these observations suggest that the actual permeability of the EDZ must be changing with time. The likely processes behind the varying permeability are swelling of the claystone and hydromechanical effects on fracture permeability due both to changes in water pressure and changes in packer pressure.

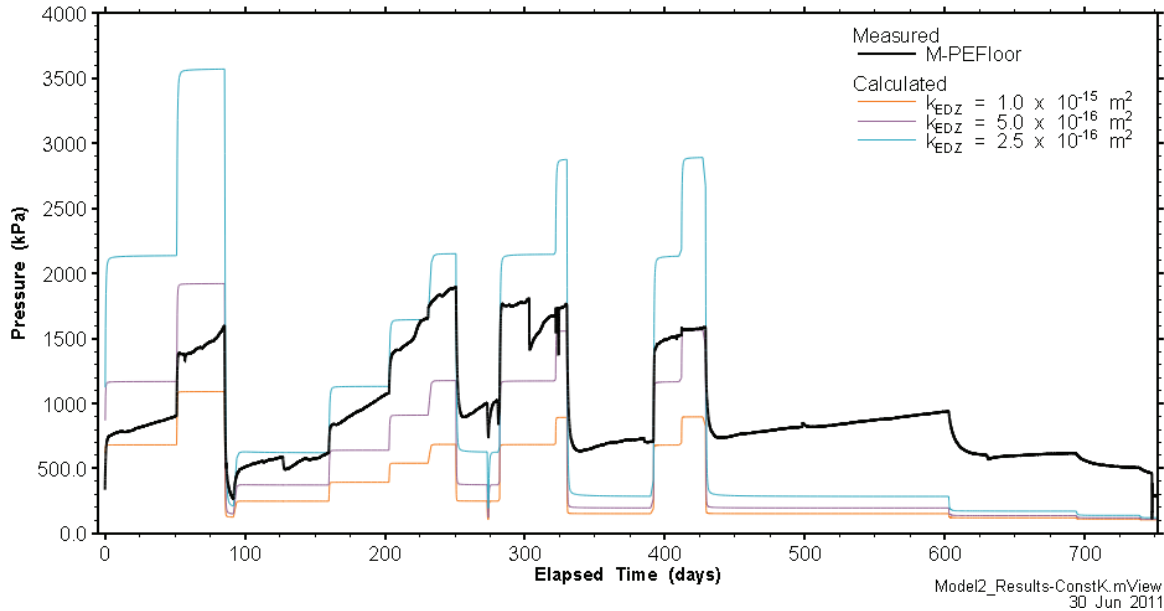


**Figure 3-13: Measured and Modelled Test Zone Pressures During the Multi-rate Hydraulic Test, Constant EDZ Permeability Models**

### 3.3.1.2 Water Flow Model: Variable EDZ Permeability

In Section 3.2.1.4 a simple calculation used to estimate the time-variable permeability was presented. This time-dependent permeability function (see Figure 3-6) was implemented in the 2D numerical model of the experiment, and the results are presented in Figure 3-14. It is clear from the figure that using the time dependent permeability function and the measured injection rates resulted in a remarkable model fit to the observed test zone pressures. Taken together with the results from Section 3.3.1.1, this suggests that the only possible way to correctly model this hydraulic test is with a non-constant permeability. It also suggests that the assumptions made when generating the permeability function (see Section 3.2.1.4) provide an adequate (if incomplete) conceptual model of what is actually happening in the HG-A test zone.

These results are successful, and show that the calculation of the permeability curve was reasonably accurate. This curve is likely affected by two distinct processes caused by the flow of water through the EDZ: (1) swelling of the damaged rock in the presence of water and subsequent healing of fractures resulting in a steady reduction in the permeability of the damaged zone; and (2) hydromechanical coupling as changes in pore pressure and confining stress leading to sometimes rapid changes in permeability. The results show that a very simple conceptualisation of the HG-A system was able to reproduce experimental observations to a significant degree. The results also show that in the presence of water the excavation damaged zone in Opalinus clay underwent significant self-healing within two years.

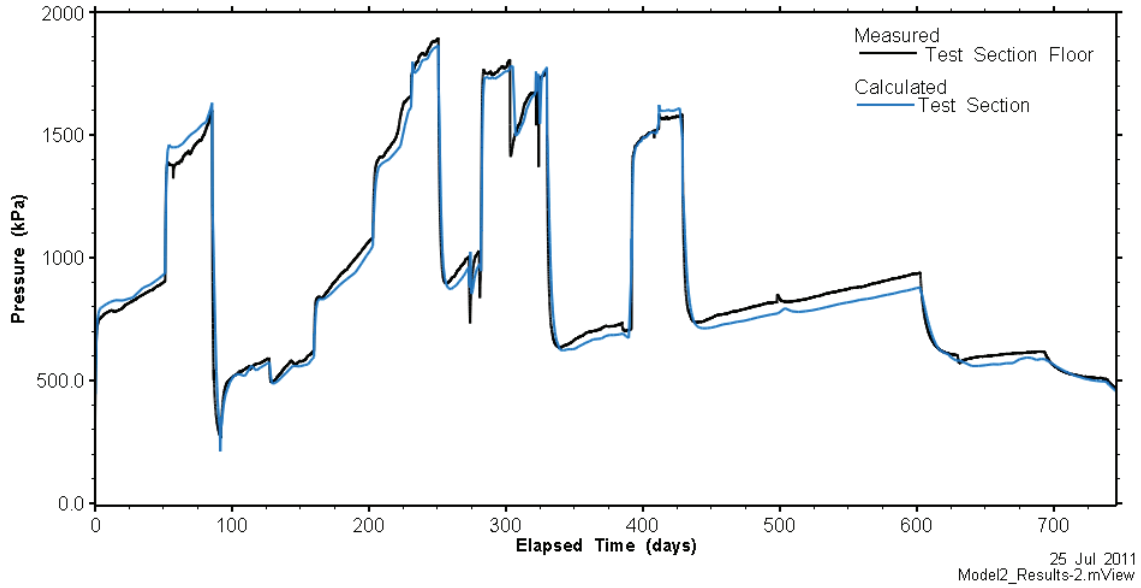


**Figure 3-14: Measured and Modelled Test Zone Pressures During the Multi-rate Hydraulic Test, 2D Variable EDZ Permeability Model**

### 3.3.2 3D Model Results

The 3D Model is a more geometrically accurate representation of the HG-A experimental geometry and arrangement. This model allows us to assess all aspects of two-phase flow in the HG-A system, including the interaction of gas buoyancy and the localisation of permeable channels in the excavation damaged zone.

#### 3.3.2.1 Hydraulic Test (Water Only)

The modelled pressures compare very well with the measured pressures in the test zone. Test zone pressure results are shown in Figure 3-15. The results for the hydraulic tests are very similar to those seen in the 2D model (Section 3.3.1.2). This provides some confidence that both models perform as expected.

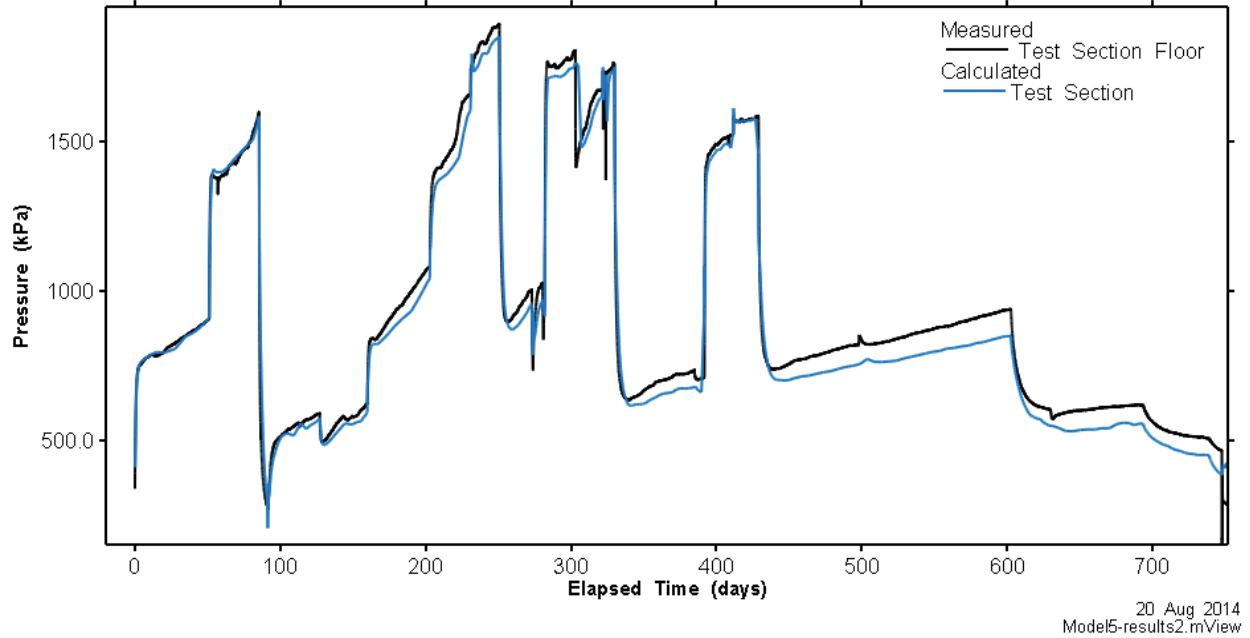


**Figure 3-15: Measured and Modelled Test Zone Pressures During the Multi-rate Hydraulic Test, 3D Variable EDZ Permeability Model**

### 3.3.2.2 Gas Test 1

Unlike the Hydraulic Test model, the Gas Test 1 model is a constant permeability model. Only a minor amount of gas escaped the test zone during this test. Pressure was primarily dissipated by water escaping through the EDZ and channel. Results for Gas Test 1 are shown in Figure 3-16. The model was able to match test zone pressure quite well.

At the packer-wall interface, the modelled pressures were not as well reproduced. At 3 and 9 o'clock the shape of the curves was similar, but the pressure loss along the packer was different. At 6 and 12 o'clock the measured pressure signals were more attenuated than modelled pressures. The differences between observed and modelled pressures at the packer-wall interface are likely due to heterogeneity of the interface/EDZ permeability not present in the model. A model with more heterogeneity would likely better fit the measurements, and require substantially more calibration effort, without providing additional useful information.

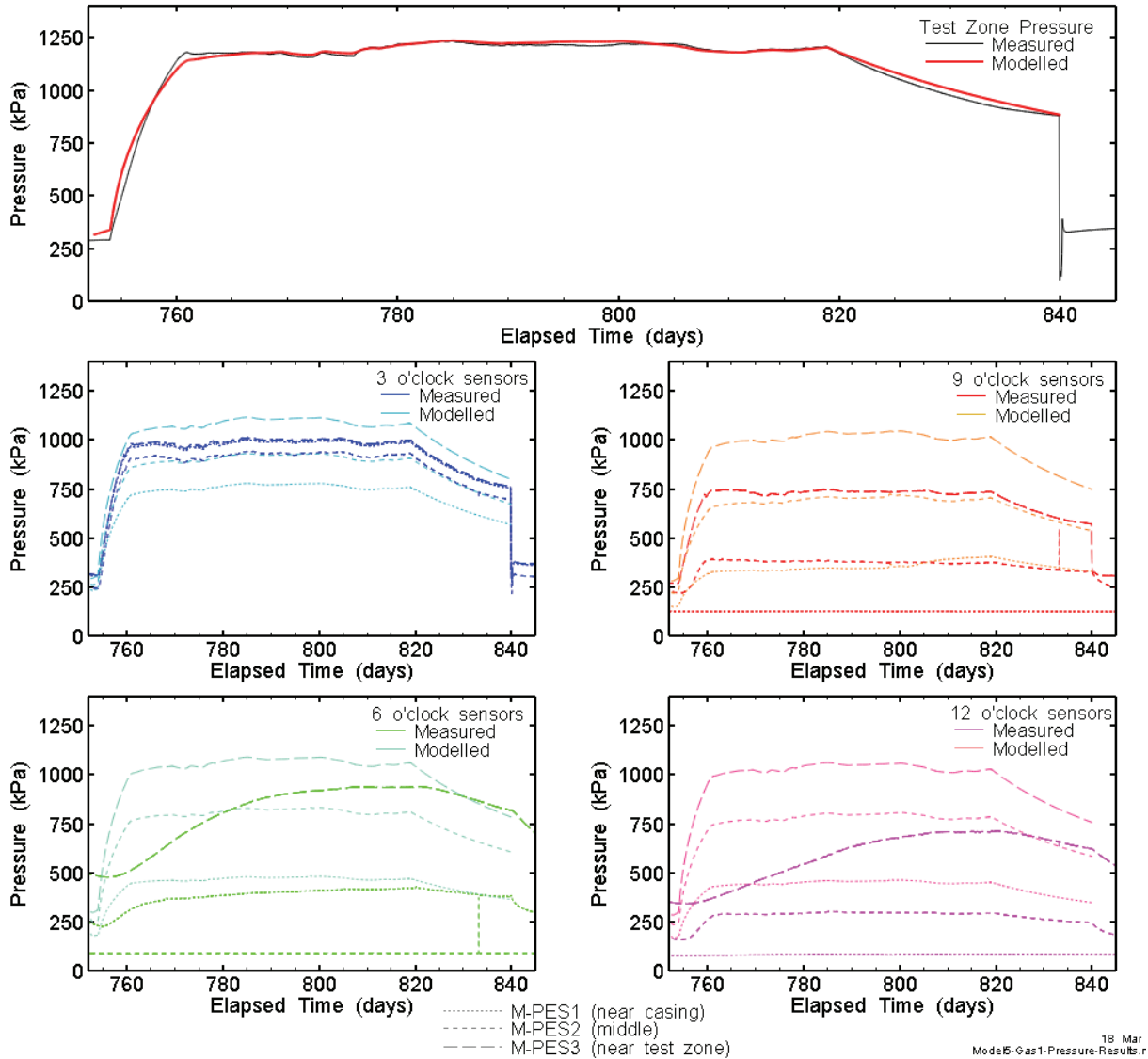


**Figure 3-16: Measured and Modelled Test Zone and EDZ Pressures for Gas Test 1**

### 3.3.2.3 Gas Test 2

The Gas Test 2 model is a constant permeability model. Results for Gas Test 2 are shown in Figure 3-17. In Gas Test 2, the pressure increased until approximately day 900 (11/07/2010), at which point, there was a sudden change in the trend and pressures begin decreasing. At day 950, the pressure appeared to reach a steady state and pressures were maintained almost constant until gas shutoff at day 1009. The decline in test section pressure coincided with the formation of a continuous gas pathway through the channel. This allowed the gas to flow freely through the channel without the need to displace any water. Once again, the modelled pressures compare well with the measured pressures in the test zone, but not along the packer-wall interface.

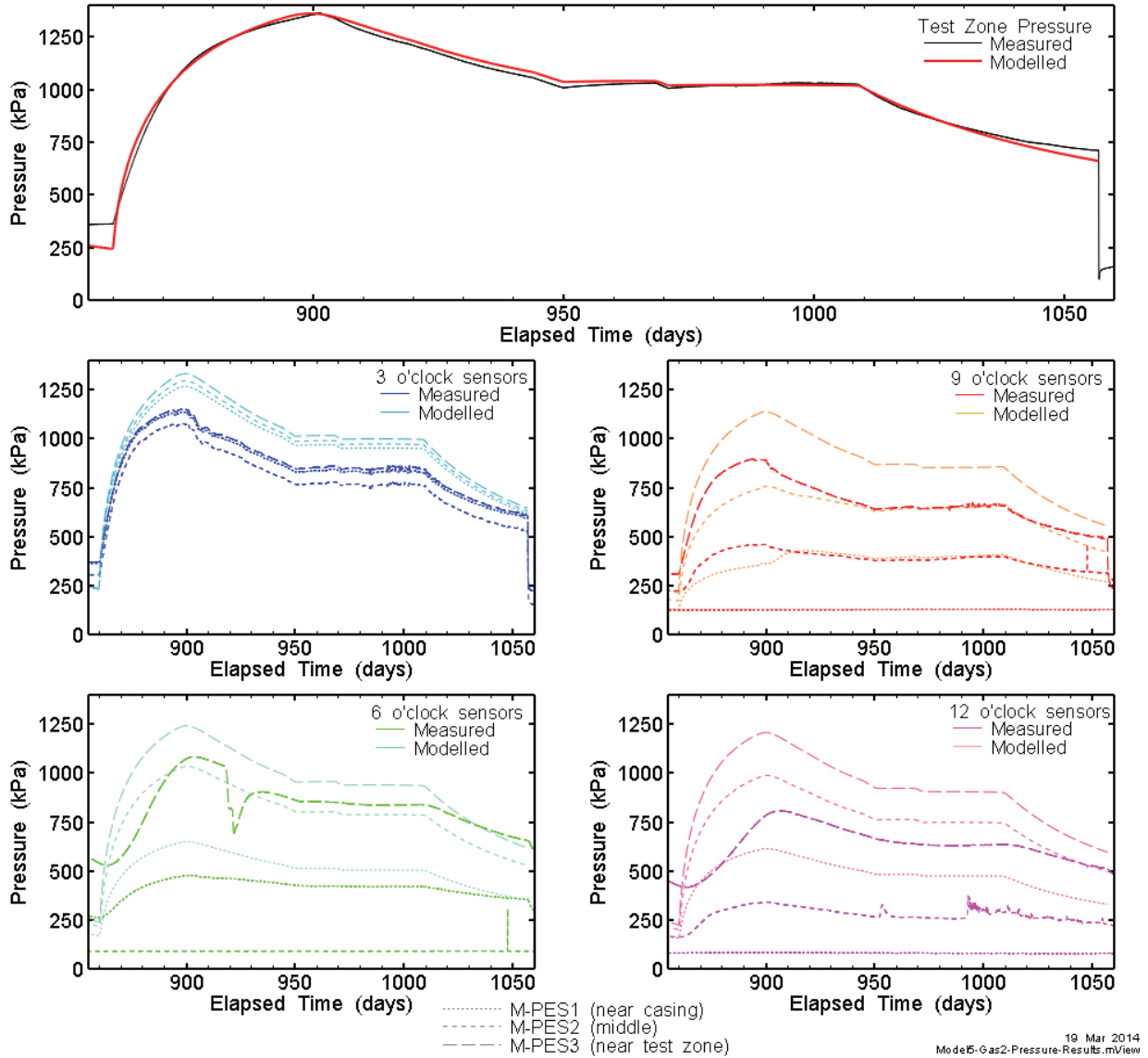


**Figure 3-17: Measured and Modelled Test Zone and EDZ Pressures for Gas Test 2**

### 3.3.2.4 Gas Test 3

Gas Tests 2 and 3 had approximately the same maximum pressure, and took approximately the same amount of time to reach that pressure, despite the fact that the injection rate for Gas Test 3 was double that of Gas Test 2. In order to replicate this behaviour, it was necessary to raise the test zone compressibility by a factor of almost three. While this change was able to match the peak pressure, it still overestimated the pressure before the peak. This suggests that a change has occurred between the two tests, perhaps incomplete flushing of gas from the previous test.

Furthermore, once the gas formed a continuous path through the channel and pressure breakdown occurred, the constant permeability model overestimated pressure (Figure 3-18 top

figure, dashed blue line), and a time varying permeability (Figure 3-18 top figure, green line) was needed in order to match the pressure (Figure 3-18 top figure, red line). At day 1247, the slope of the pressure decay curve abruptly increased. There were no changes in packer pressure or pumping rate at this time, so this event has been interpreted as the development of a new connected gas pathway, and modelled by increasing the permeability of the permeable channel. The test section pressure was on a downward trend when the gas injection was nearly stopped between days 1267 and 1269. On day 1269 the gas injection was resumed at the same injection rate as before. Pressure began to rise, and reached equilibrium at a pressure higher than where it was at the time injection ceased on day 1267. This has been interpreted as an unstable gas pathway that closed during the two days that the gas injection was interrupted. This event was modelled as a drop in permeability at this time. The results for Gas Test 3 are shown in Figure 3-18 along with the permeability scaling factors used in the model.

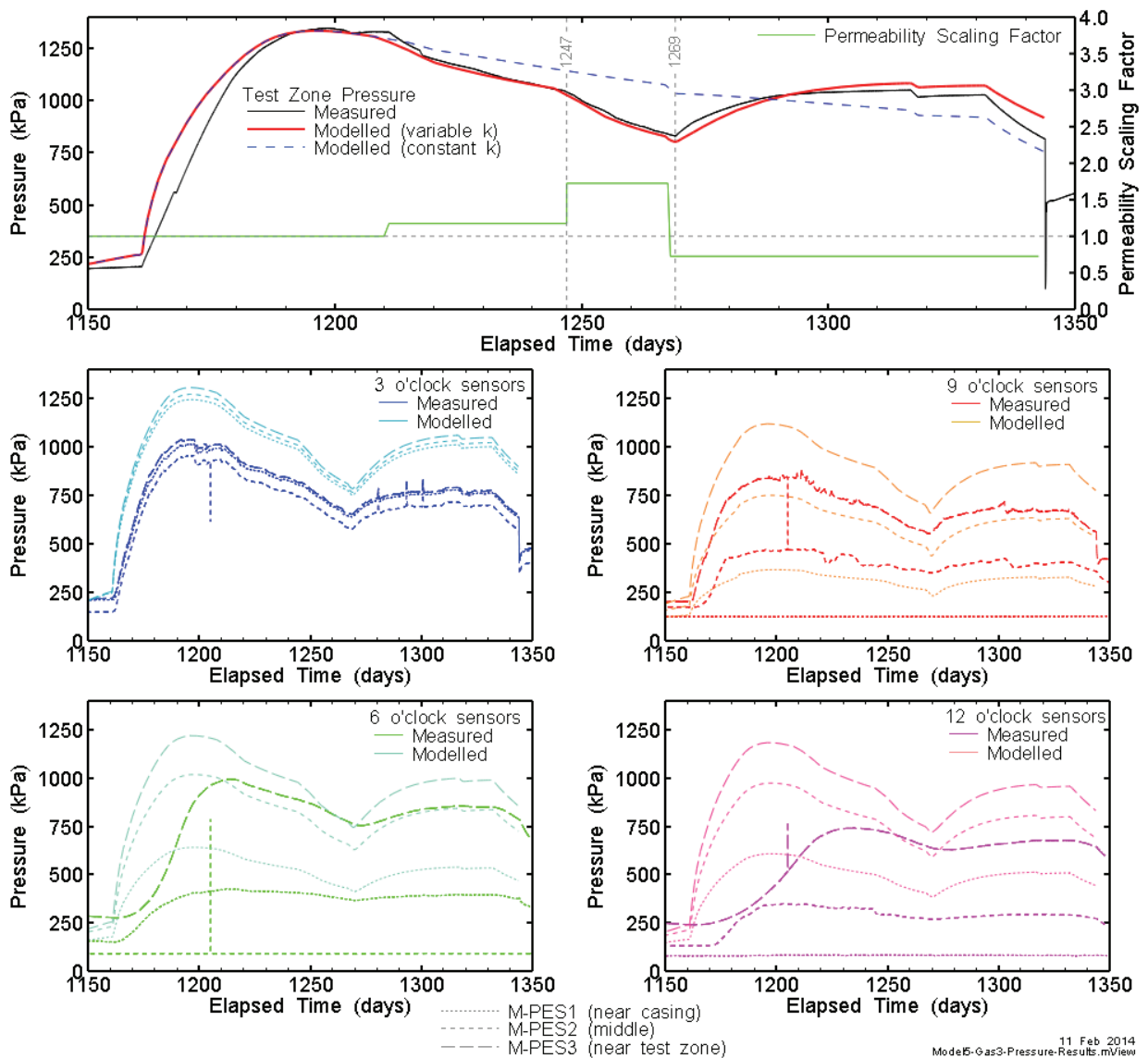
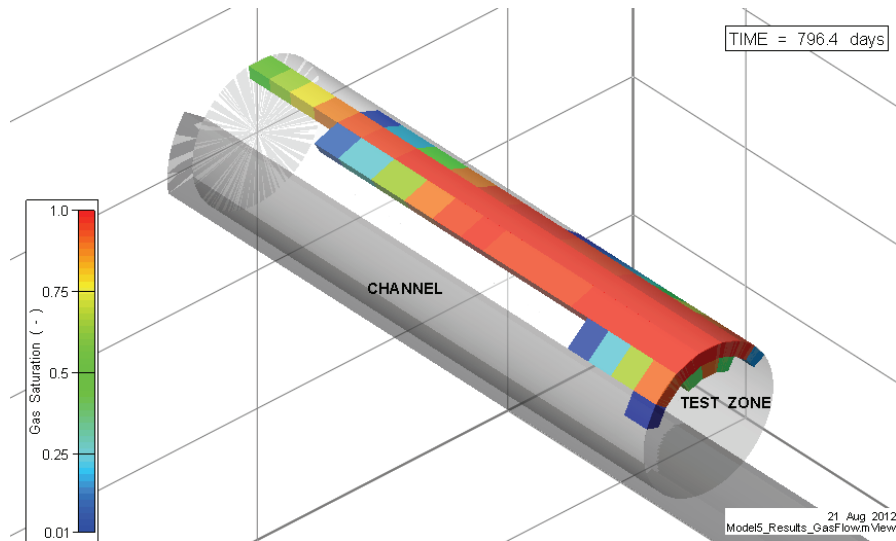


Figure 3-18: Measured and Modelled Test Zone and EDZ Pressures for Gas Test 3

### 3.3.2.5 Gas Flow Discussion

All three gas injection tests followed a similar pattern of gas flow. Initially, the injected gas pooled at the top of the test zone (see Figure 3-19) and remained largely trapped within the test zone. A small amount of gas escaped into the EDZ directly above the gas pool. Eventually, the pool of gas reached a depth where it could begin entering the channel. The channel quickly filled with gas up to a saturation where the capillary pressure was no longer zero. Physically, this would represent gas filling the fractures in the channel. Once the channel formed a continuous gas pathway to the boundary, there was a pressure breakdown as gas flowed out of the test zone faster than it was being injected. Typical gas saturations outside the test zone are shown in Figure 3-20.



**Figure 3-19: Sample Gas Saturation Showing Close-up on Test Zone with Gas Pool at the Top**

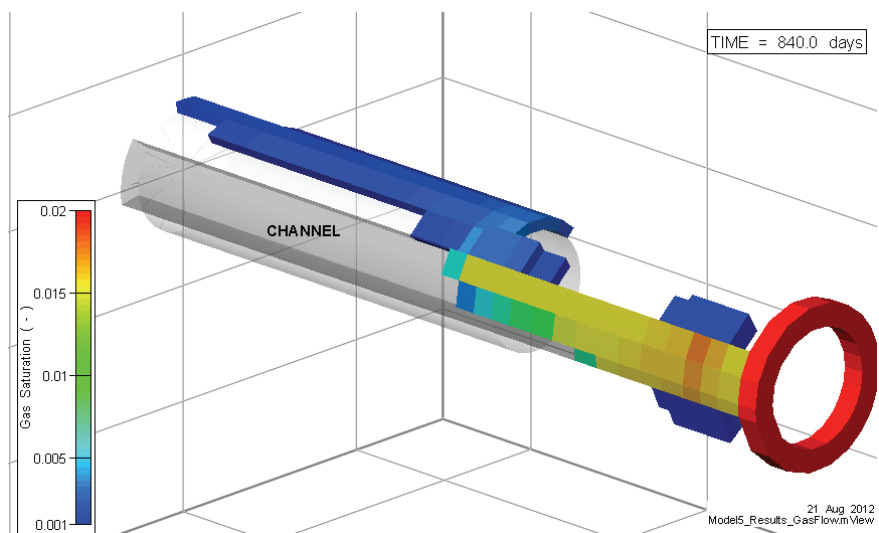


**Figure 3-20: Sample Gas Saturation Outside Test Zone with Red Ring Representing Atmospheric Boundary**

## 4. HYDRO-MECHANICAL MODELLING

Although the T2GGM models worked well to reproduce observed pressures, they could not directly model the primarily mechanical processes governing EDZ permeability. To allow us to consider mechanical processes, we investigated the TOUGH-FLAC algorithm developed at LBNL by Rutqvist and Tsang (2003), which couples TOUGH2 and FLAC3D. This algorithm leverages the strengths of each code; two-phase flow is simulated in TOUGH2, while mechanical processes are handled by FLAC3D.

To use TOUGH-FLAC for the HG-A problem, Geofirma made major changes to the original TOUGH-FLAC algorithm. Processes modelled include damage induced permeability changes, time dependent permeability reduction through swelling, and leakage around the packer system as a function of effective stress on the packer-rock interface. The hydromechanical modelling focused on the Water Flow stage, as this stage included the most interesting hydromechanical processes. The gas injection tests were not modelled using the hydromechanical model because during the Gas Flow stages, swelling processes were nearing completion, and packer pressures were kept fairly constant (Figure 2-5).

### 4.1 CODE USED

For this project Geofirma made major changes to the original TOUGH-FLAC algorithm, drawing upon the techniques developed for the 1D hydromechanical capability added to T2GGM for glaciation modeling (Walsh et al. 2012). The modified TOUGH-FLAC algorithm was incorporated within T2GGM, resulting in a coupled T2GGM-FLAC model. The T2GGM-FLAC model uses FLAC3D version 5.01, a three-dimensional explicit finite-difference program for engineering mechanics computation (Itasca 2012) used by T2GGM-FLAC to calculate damage and deformation.

Figure 4-1 illustrates the T2GGM-FLAC algorithm. In this simulator, the main external loop is controlled by T2GGM, which is responsible for solving flow processes. At each time step, the T2GGM model updates the pore pressure distribution. T2GGM then calls a subroutine to run FLAC3D using the updated pressures. These pore pressures ( $p$ ) are passed from T2GGM to FLAC3D using a script written in FLAC3D's FISH scripting language (Itasca 2012). The updated pore pressures result in changes in effective stresses and a new equilibrium state in FLAC3D. Based on these values, FLAC3D assesses the resulting deformation and damage. These mechanical processes cause changes to the porosity ( $\phi$ ) and permeability ( $k$ ), which are updated, returned to the external T2GGM loop, and used to resume the flow solution. This approach allows us to simulate both the damage resulting from excavation and due to changes in pore pressure. Other processes included in the model are swelling (time dependent) and leakage around the packer (as a function of effective stress at the packer-rock interface).

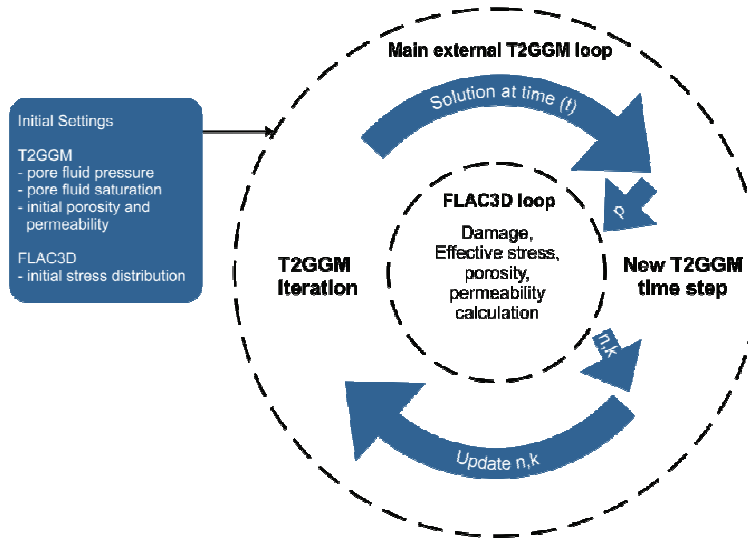


**Figure 4-1: T2GGM-FLAC3D Simulator Algorithm**

## 4.2 CONSTITUTIVE MODELS

In this section the basic constitutive models for plastic failure and hydro-mechanical coupling are described.

### 4.2.1 Elasto-Plastic Mechanical Model

To model damage due to stress redistribution around the HG-A tunnel (i.e., the development of the EDZ) the Ubiquitous-Joint Model (UJM) was used. This model accounts for the elasto-plastic behaviour of the anisotropic (bedded) Opalinus clay by modelling it as a Mohr-Coulomb solid with weak planes at a specific orientation. The UJM algorithm assesses two separate failure criteria. The first is the general composite Mohr-Coulomb failure criterion in all orientations; the second is the specific (weaker) composite Mohr-Coulomb envelope at the specified angle of the weak plane. In total four modes of failure are assessed: (1) shear failure in the intact rock, (2) tension failure in the intact rock, (3) bedding plane shear failure, and (4) bedding plane tensile failure.

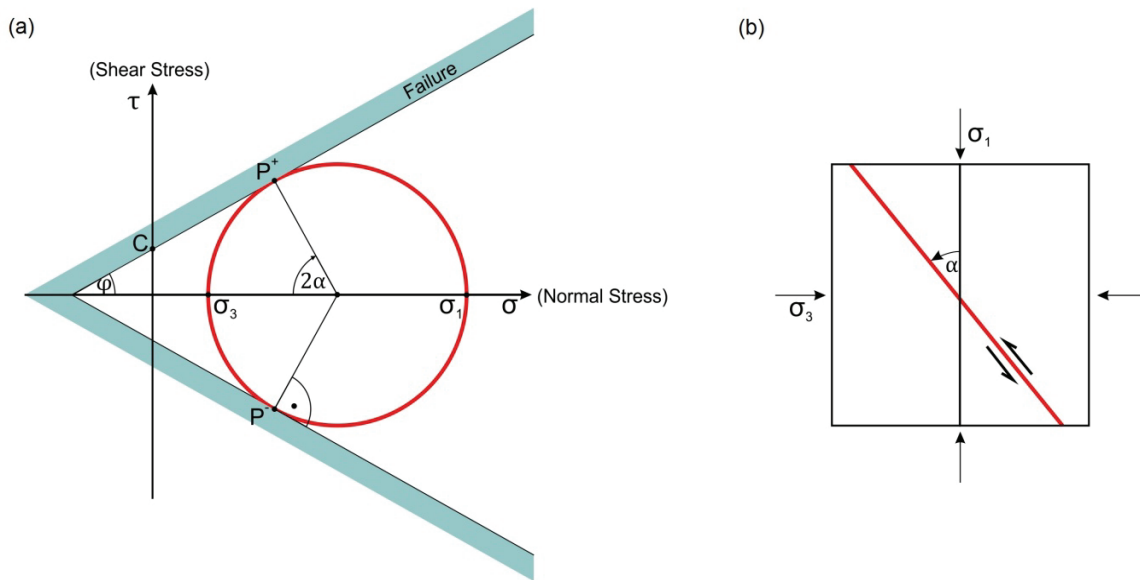
The failure envelope of the composite Mohr-Coulomb Model is a shear yield function with tension cut-off (tension yield function) expressed in terms of the principal effective stresses. The general form of Mohr-Coulomb Model relates the shear strength to the applied normal effective stress as shown in the following equation (see also Figure 4-2).

$$\tau_s = C + \sigma_n \tan \varphi \quad (3)$$

Where:  $\tau_s$  = the shear strength;

$\sigma_n$  = the effective<sup>1</sup> normal stress;  
 $C$  = the cohesion; and  
 $\varphi$  = the angle of internal friction.

For the composite Mohr-Coulomb model, there are two components to the failure envelope, shear failure  $f^s$  and tensile failure  $f^t$ . Figure 4-2 shows the generalized Mohr-Coulomb shear failure model. Shear failure in the rock occurs when the principle stress circle (red circle) touches the failure line (points  $P^\pm$ ). Although Figure 4-2 shows positive and negative shear stresses, in practice it is the absolute value of the shear stress that determines failure. This analysis also provides the orientation of the failure plane ( $\alpha$ ).



Note: Tension is traditionally defined as negative in this plot.

**Figure 4-2: Generalized Mohr-Coulomb Shear Failure Model: (a) Mohr Circle and Mohr-Coulomb Failure Criterion on a Shear Stress- Normal Stress Plot (after Zang and Stephansson 2010); (b) Failure Plane Orientation in Laboratory Tests**

The critical limit that defines the state of shear failure ( $f^s$ ) is the failure envelope function, a function of the maximum and minimum effective principle stresses ( $\sigma_1$  and  $\sigma_3$ ), the cohesion  $C$ , and the angle of internal friction  $\varphi$ :

$$f^s(\sigma_1, \sigma_3, C, \varphi) = \sigma_1 - \sigma_3 N(\varphi) + 2C\sqrt{N(\varphi)} = 0 \quad (4)$$

<sup>1</sup> Note that effective stress is simply the total stress minus the pore pressure. In T2GGM-FLAC pore pressures are calculated in T2GGM.

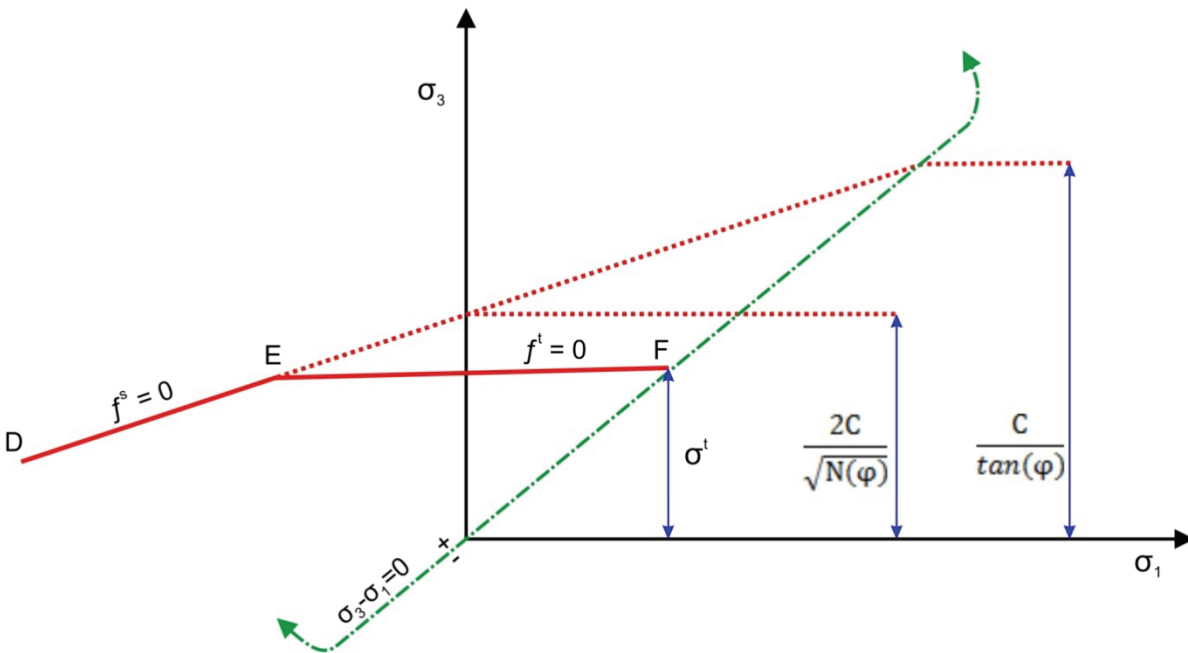
$$N(\varphi) = \frac{1 + \sin(\varphi)}{1 - \sin(\varphi)} \quad (5)$$

In these equations,  $\sigma_1$  and  $\sigma_3$  are negative in compression as defined in FLAC3D.

If tensile stresses are created by redistribution of stress due to excavation, the rock will fail by tensile fracturing rather than shear if the magnitude of the tensile stress ( $\sigma_3$ ) equals or exceeds the tensile strength of the rock. The tension yield function ( $f^t$ ) can be expressed as a function of the minimum effective principle stress ( $\sigma_3$ ) and the tensile strength of the material ( $\sigma^t$ ) as shown in the following equation (Itasca 2012):

$$f^t = \sigma_3 - \sigma^t \quad (6)$$

The model tests for plastic failure using both  $f^s$  and  $f^t$ . It is possible for the material to be in failure in both tension (on one plane) and shear (on a different plane). Figure 4-3 shows the composite of Mohr-Coulomb shear criterion (line DE) with a tension cutoff (line EF) on a  $\sigma_3, \sigma_1$  plot. In Figure 4-3 compression is defined as negative.



Note: Tension is defined as positive in this plot.

**Figure 4-3: UJM Composite Mohr-Coulomb Model Failure Envelope for Intact Rock (After Itasca 2012)**

As stated earlier, the second failure criterion tested by the UJM is the specific (weaker) bedding plane yield function. For this purpose, the general form of the Mohr-Coulomb Model is applied

on the bedding plane using the stress components on the joint plane ( $\sigma_{nj}$ ,  $\tau_j$ ). The shear failure envelope of the bedding Mohr-Coulomb criterion ( $f_j^s$ ) is shown in the following equation:

$$f_j^s = \tau_j - \sigma_{nj} \tan(\varphi_j) - C_j \quad (7)$$

Where:  $\sigma_{nj}$  = the effective normal stress on the bedding plane, calculated by rotating the effective principle stresses using the dip and direction of the bedding plane (therefore, it is a function of dip, direction,  $\sigma_1$ , and  $\sigma_3$ );

$\varphi_j$  = the angle of internal friction on bedding plane;

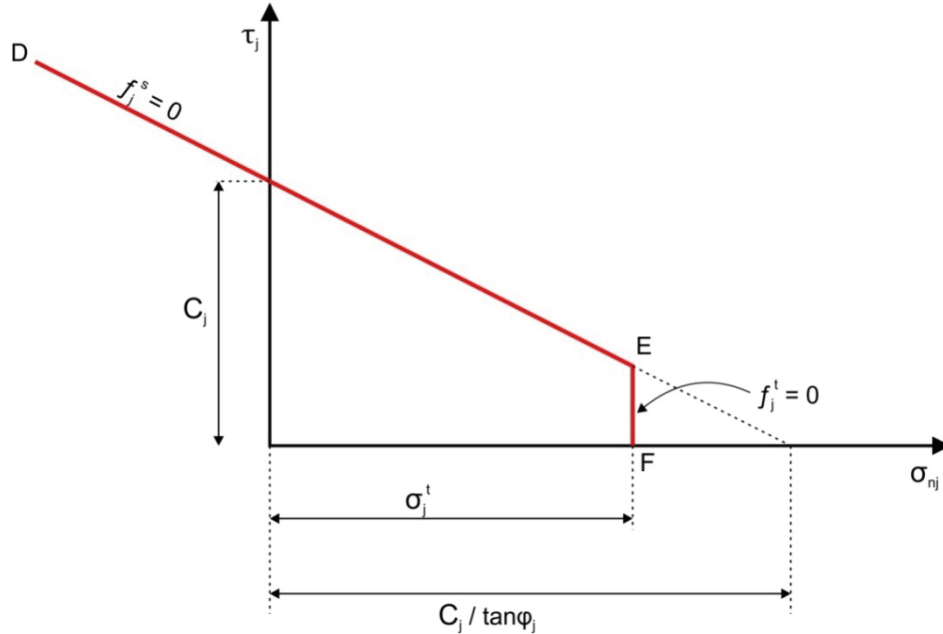
$C_j$  = the cohesion of the bedding plane; and

$\tau_j$  = the magnitude of the tangential traction component on the bedding plane.

As with the general failure criterion, the bedding yield function has a tension cutoff ( $f_j^t$ ), which can be expressed as a function of  $\sigma_{nj}$  and the tensile strength of the bedding plane of the material ( $\sigma_j^t$ ) as shown in the following equation:

$$f_j^t = \sigma_{nj} - \sigma_j^t \quad (8)$$

Figure 4-4 shows the composite of bedding Mohr-Coulomb shear criterion (line DE) with bedding tension cutoff (line EF) on a ( $\sigma_{nj}$ ,  $\tau_j$ ) plane.



Note: Tension is defined as positive in this plot.

**Figure 4-4: Ubiquitous-Joint Model Composite Mohr-Coulomb Failure Envelope for Bedding Planes (After Itasca 2012)**

#### 4.2.2 EDZ Damage and Permeability

As described in Section 4.2.1, four types of plastic deformation were calculated based on the mode of failure. The extent of the EDZ is evaluated based on the plastic shear failure state as follows: (1) no failure, (2) shear failure in the intact rock, (3) tension failure in the intact rock, (4) bedding plane shear failure, and (5) bedding plane tensile failure. As we do not have laboratory-scale data connecting degree of damage or failure mode to changes in permeability, it was necessary to propose a function for the damage-stress-permeability relationship and then calibrate the coefficients of the function by comparing model predictions of test zone pressure to experimentally determined values. The form of the proposed equation is as follows:

$$\log k_d = A + B e^{C\sigma_{avg}} \quad (9)$$

$$\sigma_{avg} = \frac{\sigma_1 + \sigma_2 + \sigma_3}{3} \quad (10)$$

Where:  $\sigma_{avg}$  = average *effective* stress (Pa), which in the HG-A experiment changes as packer pressure or pore pressure changes.

The coefficients  $A$ ,  $B$ , and  $C$  are fitting parameters, calibrated using test zone pressures. Parameter  $A$  (-17.06) represents a residual or irreducible permeability present at high stresses. Parameter  $B$  is a function of the failure mode (see Table 4-1 for calibrated values). This parameter controls the degree of post-damage permeability increase when confining stress declines to zero. This increase over the residual permeability exponent ( $A$ ) is equal to  $B$  when the applied stress is zero (exponent is zero, and  $\log k_d = A + B$ ). Parameter  $C$  ( $5 \times 10^{-8}$ ) controls the slope of the permeability-stress relationship. As parameter  $C$  increases, the permeability drops more rapidly with rising confining stress. The form of Equation (9) is similar to that suggested by Popp et al. (2008) and authors studying basin scale or subglacial compaction (Bethke and Corbet 1988, Person et al. 2012). It is also in agreement with laboratory scale measurements of stress permeability-coupling in single fractures (Walsh et al. 2008, Davy et al. 2007). Figure 4-5 shows measurements of permeability of single fractures under increasing applied load and the damaged zone permeability as described in Equation (9). The measured laboratory-scale fracture permeability-stress relationships shown in Figure 4-5 could be fit using Equation (9) and an appropriate selection of fitting parameters. Given that the enhanced permeability in the damaged zone is likely a consequence of fracturing, it is reasonable to assume that stress-permeability coupling in the EDZ will follow a similar pattern to the measured behaviour of single fractures in laboratory-scale samples.

**Table 4-1: Failure Mode and Corresponding Estimated Change in Parameter  $B$**

Failure State	Equation (9) Parameter $B$
Failure in shear	
Failure in tension	
Failure in bedding plane shear	2.96
Failure in bedding plane tension	
Combination of more than one of the above	3.52

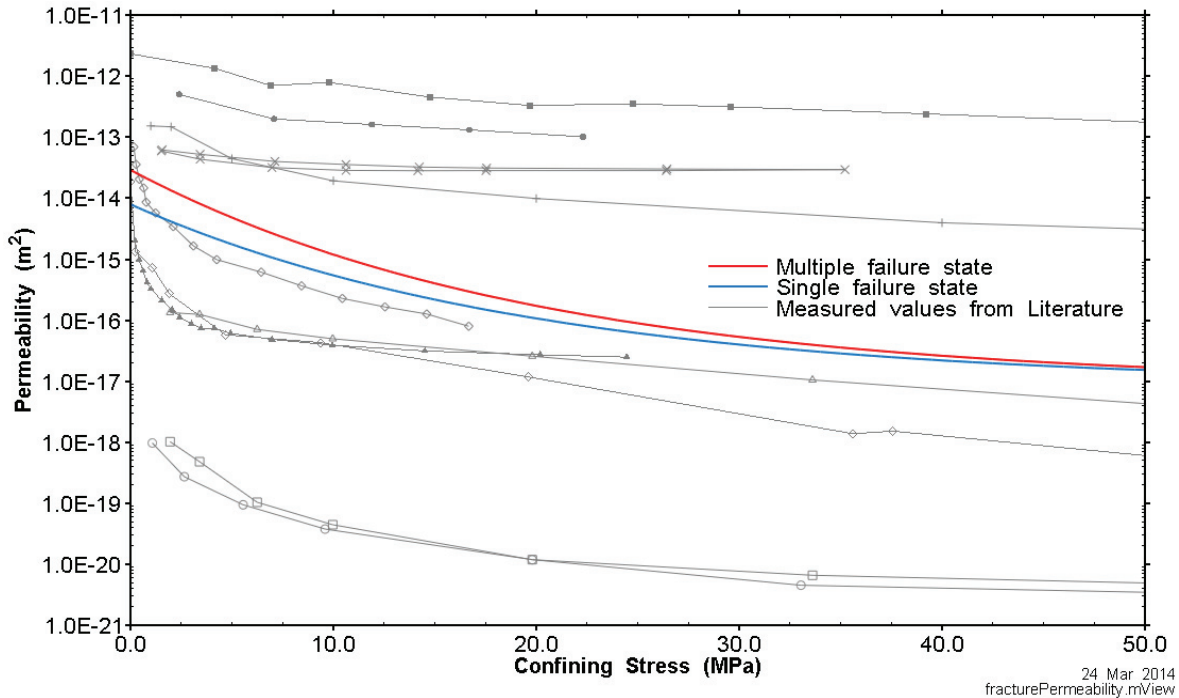


**Figure 4-5: Measured Stress-Permeability Relationships for Single Rock Fractures (Walsh et al. 2008) Compared to HG-A Damaged Zone Stress Permeability Relationship**

#### 4.2.3 EDZ Swelling and Permeability

We have focused on permeability changes caused by damage, which in turn is caused by stress redistribution around the open tunnel. In the Opalinus clay, there is ample evidence that permeability may be reduced through self-sealing, primarily due to swelling of the fracture wall material (Bock et al. 2010, Lanyon 2012). The permeability change as a result of swelling (self-healing of damage zone) is modeled as an exponential decay function of time as follows:

$$k = k_d e^{D(t-t_0)} \quad (11)$$

Where:  $D$  = a fitting parameter controlling the rate of permeability decay with time ( $-5 \times 10^{-8}$ );  
 $k_d$  = the damaged permeability ( $m^2$ ) from Equation (9);  
 $t_0$  = the time of swelling initiation (s) (in this case the start of modelling); and  
 $t$  = the current time (s).

Parameter  $D$  was calibrated using the test zone pressure curve.

The choice of an exponential decay function for EDZ permeability as a function of time-dependent swelling was based on the estimated baseline permeability shown in Figure 3-6. The shape of the curve described by Equation (11) is similar to the estimated baseline permeability in this figure. In laboratory-scale samples of Opalinus clay, time-dependent evolution of permeability for three Opalinus clay samples with single fractures was studied by Bernier et al. (2007). Results of these experiments could be fit by Equation (11). A further study described in Bernier et al. (2007) looked at time and stress dependent changes in

permeability of an Opalinus clay sample with a small hole drilled in the centre. Similarly, this experimental study could be adequately modeled using Equations (9) and (11). These lab-scale studies of permeability evolution in damaged Opalinus clay showed behavior consistent with this mathematical approach, although parameters used to fit these laboratory-scale experiments were different from field-scale fitting parameters.

In laboratory studies on Callovo-Oxfordian argillite Davy et al. (2007) observed that the relationship between confining stress and permeability was greatly reduced over time in the presence of water. By the end of the experiment the permeability was equivalent to that measured on samples of intact argillite, and was independent of confining stress. They interpreted this as a consequence of swelling which closes and fills the fracture with argillite sludge, sealing it entirely. In this work, the swelling-dependent attenuation of the stress-permeability relationship has not been modelled.

#### 4.2.4 Packer Interface Permeability and Boundary Conditions

The packer was installed to close the gap at the packer-rock interface, forcing any liquid and/or gas leaking from the test zone to flow through the EDZ. The packer performance (or efficiency) is dependent on the packer pressure, but is also on the pore pressure at the packer-rock interface. If the pore fluid pressure exceeds the packer pressure, this should cause the interface between the rock wall and the packer to open up, letting fluids leak out of the test zone and bypass the EDZ. Figure 4-6 shows the test zone fluid pressure and the average packer pressures at two circumferences — M\_TPS1 and M\_TPS2<sup>2</sup>. During the hydraulic test there were two times when the test zone pressure approached or surpassed the average measured total stress at the packer-rock interface. These correspond to times when the apparent permeability of the EDZ is elevated according to the analysis described in Section 3.2.1.4 (see also Figure 3-6). This suggests that water is very likely leaking along the interface, rather than flowing through the EDZ.

The effective stress-dependant performance of the packer-rock interface was simulated by a 1.5 cm thick layer along the tunnel wall, for which permeability ( $k_{int}$ ) was calculated as a function of applied effective packer pressure ( $\sigma'$ ) as shown in the following equation:

$$\log_{10} k_{int} = \log_{10} k_{ref} - F(\sigma_{ref} - \sigma') \quad (12)$$

Where:  $k_{ref}$  = the reference permeability ( $m^2$ ); and  
 $\sigma_{ref}$  = the effective stress (MPa).

$k_{ref}$  was set at  $1.12 \times 10^{-20} m^2$  (the permeability of intact rock), and  $\sigma_{ref}$  was set at 2.5 MPa compression. This is slightly higher than the maximum effective stress observed during the hydraulic test experiment. The parameter  $F$  is a fitting parameter, controlling the slope of the permeability-stress relationship;  $F$  was calibrated to a value of  $2.7 \times 10^{-6}$  to better fit the data of measured versus the predicted test zone pore pressure. The packer-wall interface is akin to a fracture, for which a log-linear permeability-effective stress function like the one used here is a reasonable assumption (Walsh et al. 2008). The interface permeability function is shown graphically in Figure 4-7.

<sup>2</sup> For sensor locations, see Figure 2-1. Individual pressure curves are shown in Figure 2-2.

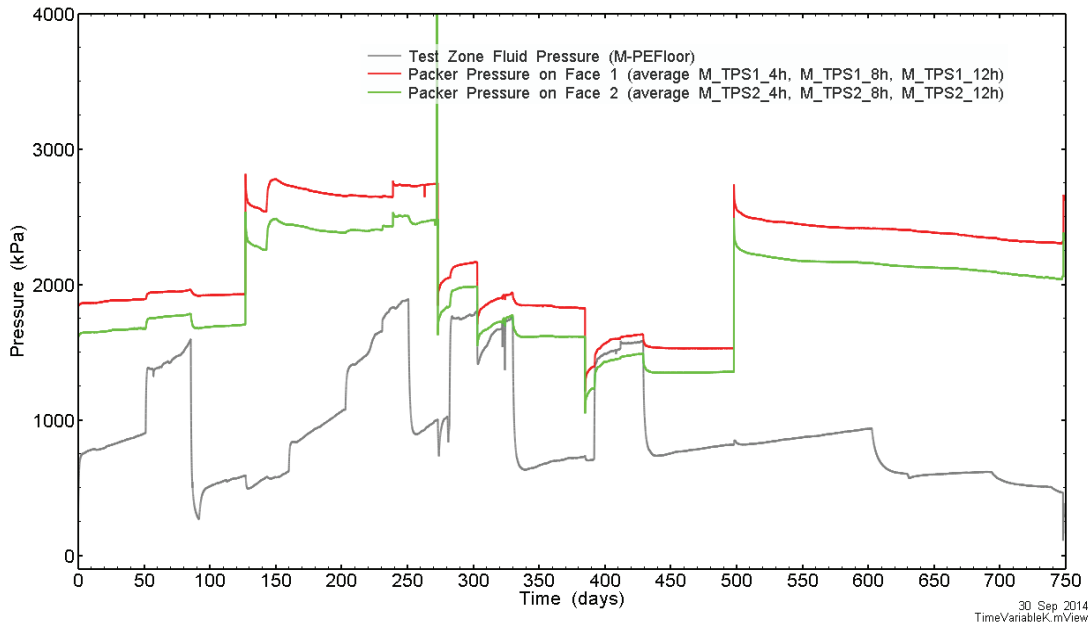


**Figure 4-6: Test Zone Fluid Pressure Compared to Average Applied Packer Pressure at the Packer-Rock Interface**

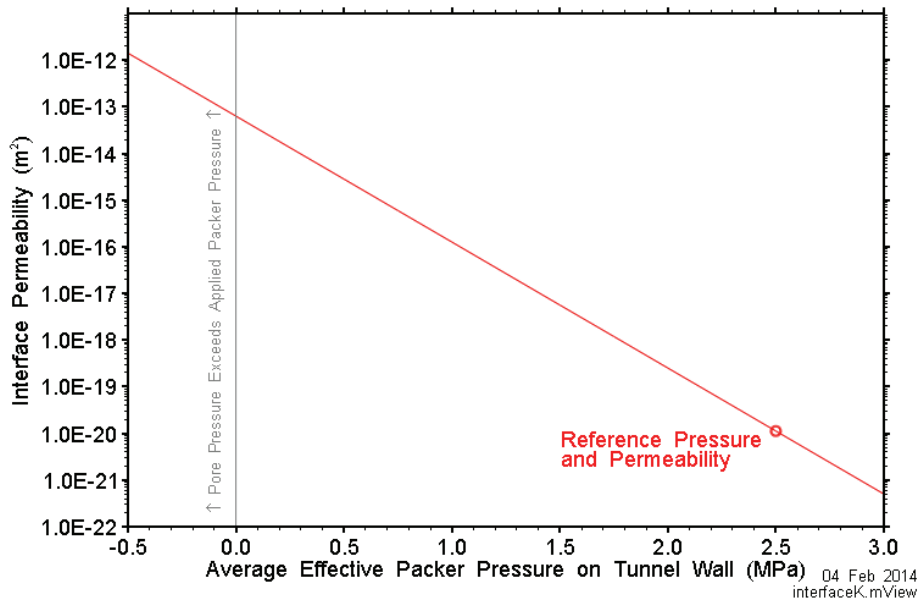


**Figure 4-7: Permeability Function for the Packer-Rock Interface**

### 4.3 MODEL SETUP

In this section the setup of the hydro-mechanical model of the HG-A experiment is described.

#### 4.3.1 Properties

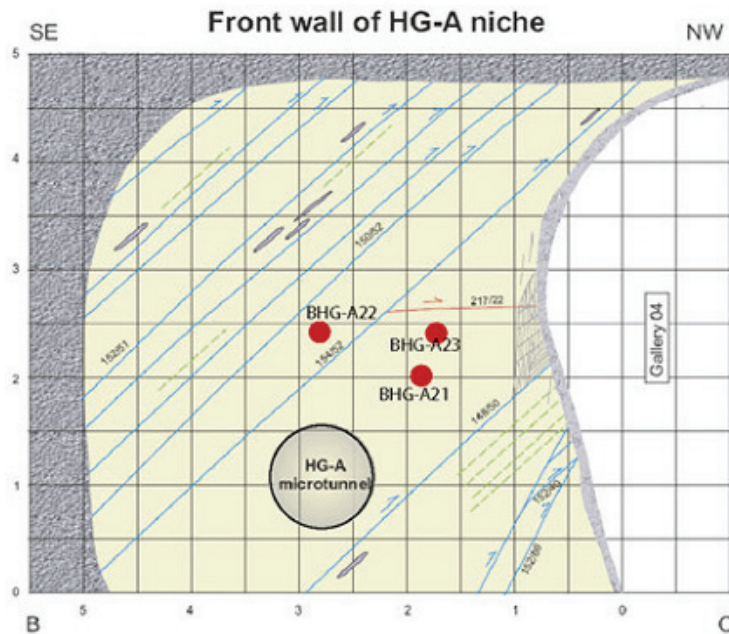
The Opalinus Clay at Mont Terri can be classified as a slightly over-consolidated rock with over-consolidation ratio of 2.5 to 3.5. From a rock mechanics perspective, an important feature of the Opalinus clay at Mont Terri is the existence of steeply dipping bedding planes, at an angle of approximately 45-50° (see Figure 4-8 and Figure 4-9). Opalinus clay is known to have reduced shearing resistance along these bedding planes (Martin and Lanyon 2003). This has been incorporated into our geomechanical conceptual model of the HG-A experiment through use of the Ubiquitous-Joint Model (UJM) described in Section 4.2.1. The UJM is used to model the elasto-plastic behaviour of the anisotropic (bedded) Opalinus clay. Input parameters for the UJM, taken from Marschall et al. (2006), were obtained from laboratory and in-situ tests (Blümling and Konietzky 2004, Bock 2001) are shown in Table 4-2.

For the T2GGM component of the model, material properties are the same as those described for the two-phase flow model in Section 3.2.2.1. Unlike the two-phase flow model, there are only two property groups: ROCK and TEST zone. There were no separate property groups for the EDZ. The extent and shape of the damaged zone is calculated by the model, and permeability of damaged material is calculated as described in Section 4.2.



Note: Photo was taken by O. Nasir, facing northeast

**Figure 4-8: Bedding Planes at the Mont Terri URL at a Location Near the HG-A Tunnel**



Note: Observer is facing HG-A tunnel, pointing approximately southwest. Red circles are stressmeter boreholes; blue lines are fault planes subparallel to bedding; red line is a fault plane; grey is shotcrete; yellow is Opalinus clay; and green dotted-lines are desaturation cracks subparallel to bedding trace.

**Figure 4-9: Illustration of Bedding Planes at the HG-A Tunnel (Corkum and Martin 2008)**

**Table 4-2: Properties for the Ubiquitous Joint Model**

Property	Value	Source
Bulk modulus, $K$ (GPa)	8.4	Marschall et al. (2006)
Elastic shear modulus, $G$ (GPa)	1.087	Calculated from Bulk modulus and Poisson's ratio
Cohesion, $C$ (MPa)	3	Marschall et al. (2006)
Rock mass density, $\rho$ ( $\text{kg}\cdot\text{m}^{-3}$ )	2450	Marschall et al. (2006)
Dilation angle, $\psi$	0	assumed
Tension limit, $\sigma^t$ (MPa)	1	Marschall et al. (2006)
Friction angle, $\phi$	39	Marschall et al. (2006)
Joint cohesion, $C_j$ (MPa)	1	Marschall et al. (2006)
Joint dilation angle, $\psi_j$	0	Assumed
Dip angle (degrees) of weakness plane	45	Corkum and Martin (2008)
Joint friction angle, $\phi_j$	34	Marschall et al. (2006)
Joint tension limit, $\sigma_j^t$ (MPa)	0.5	Marschall et al. (2006)

### 4.3.2 Model Geometry and Property Distribution

T2GGM-FLAC modelling of the HG-A experiment was carried out using a radially gridded 3D block model. The T2GGM and FLAC model used similar grids. The location of element centroids in the two grids is identical, but the shape of the elements differs slightly. This is due to a limitation of gridding algorithms available for TOUGH2. The model domain has 39,744 elements (in both T2GGM and FLAC3D), and dimensions of 20 m  $\times$  18 m  $\times$  20 m, extending 10 m into the surrounding rock perpendicular to the tunnel. Due to the bedding dip and anisotropy, symmetry could not be used to reduce the size of the model. Figure 4-10 shows a cut-away section halfway through the 3D geometry of the analysed domain. The presence of nearby access tunnels is neglected in the model.

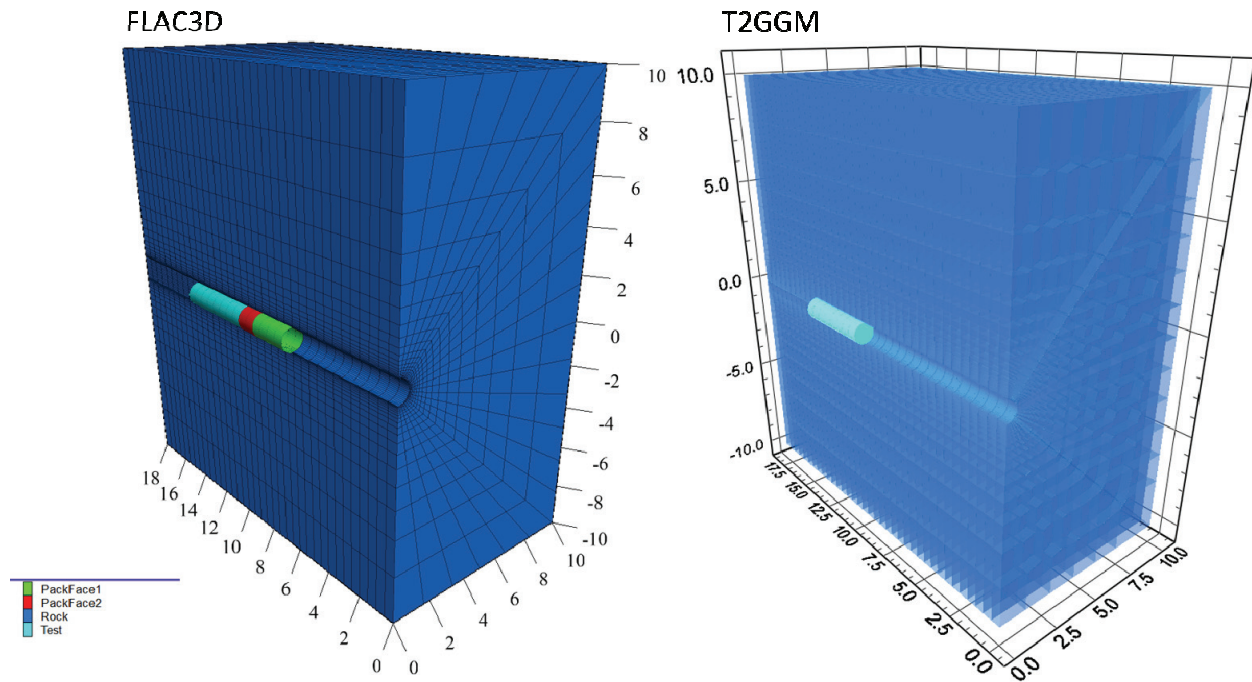


**Figure 4-10: Cut-away Cross Section through Model Domain, Comparing FLAC3D and TOUGH2 Geometry**

The FLAC3D model is comprised of four materials: Rock, Test Zone, Packer-Rock Interface 1, and Packer-Rock Interface 2. Packer-rock interface properties are distributed in a very thin layer along the tunnel wall adjacent to the packer. The reason for having a two separate packer-rock interface properties is described in the next section. Unlike the two-phase flow modelling discussed in Section 3, there is no separate property for the EDZ. The location and properties of the EDZ are a model output, calculated in T2GGM-FLAC as a result of stress redistribution, applied packer stress, time, and pore pressures (see Sections 4.4.1 and 4.4.2). Similarly, in the T2GGM part of the model there is no separate property for the packer-rock interface, as the permeability of this interface is an output from the FLAC3D model, changing as a function of the packer and pore pressure.

### 4.3.3 Initial and Boundary Conditions

In addition to the experimental data such as pressures, geomechanical modelling requires further information, much of which was provided as part of the project data packages. For geomechanical modelling, a key constraint is the local stress regime. Sources estimating the in-situ stress at the location of the HG-A tunnel include Corkum and Martin (2007) and Lanyon et al. (2009). Based on these sources the local stress regime at the level of the rock laboratory was estimated as follows:

- The maximum principal stress ( $\sigma_1$ ) is vertical, with a magnitude on the order of 6.5 MPa.
- The minimum principle stress ( $\sigma_3$ ) is NE-SW-oriented, parallel to the HG-A tunnel, and has a magnitude of 2.5 MPa.
- The intermediate principle stress ( $\sigma_2$ ) runs in a NW-SE direction, parallel to the security gallery, and has a magnitude of 4.5 MPa (see Figure 4-11) (Lanyon et al. 2009).

The orientations of the principle stresses in the context of the HG-A tunnel are shown in Figure 4-11. This stress regime is applied as a mechanical boundary condition in the FLAC3D model, and is also used to define the initial stress distribution.

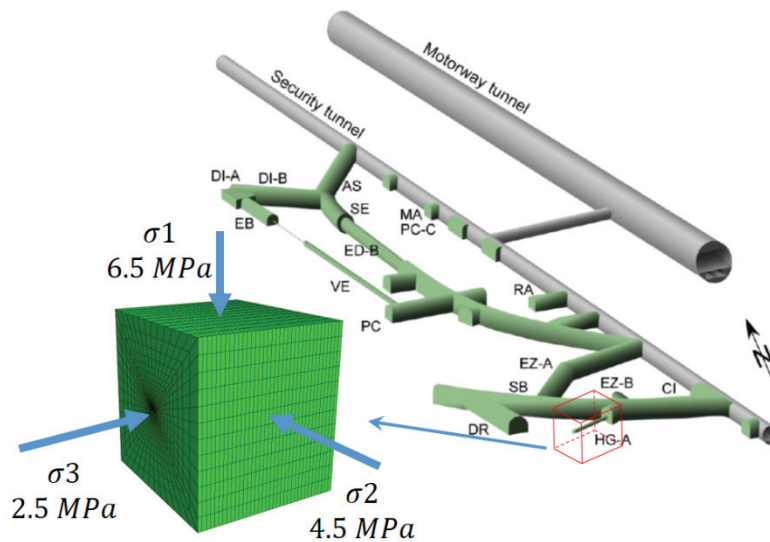


**Figure 4-11: Principle Stresses at the Level of the Mont Terri URL**

The initial pore pressure distribution is very similar to that used for two-phase flow modeling (Section 3). Figure 4-12 shows the initial pore pressure distribution used for the T2GGM-FLAC model.

For the packer-rock interface, a specified stress boundary condition normal to the tunnel surface was applied. As shown in Figure 2-2, the applied packer-rock interface pressure was not uniform in time or space. To account for the variable distribution of packer pressure, the packer zone was divided into two zones: PackFace1 and PackFace2, with a different normal stress applied to each of these zones. To these surfaces, the corresponding average pressures M-TPS1 (average of M-TPS1-4h, M-TPS1-8h, M-TPS1-12h) and M-TPS2 (average of M-TPS2-4h,

M-TPS2-8h, M-TPS2-12h) were applied (see Figure 4-6). The two interface zones are illustrated in Figure 4-13.

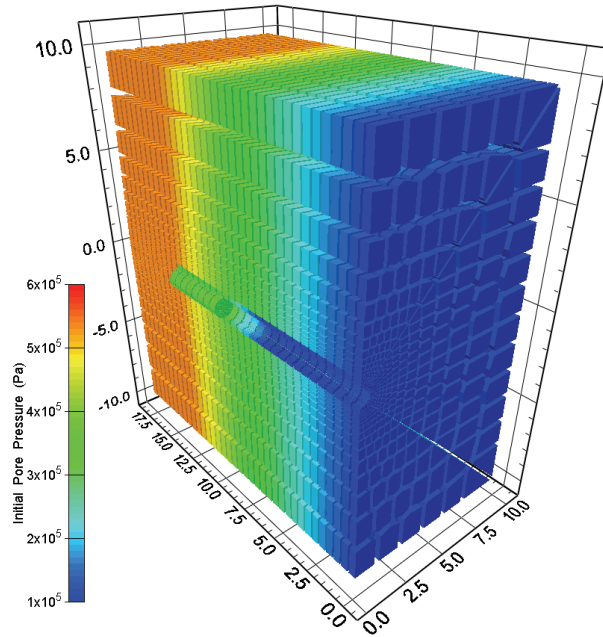


**Figure 4-12: Initial Pore Pressure Distribution (Shown Here on the T2GGM Model Grid)**

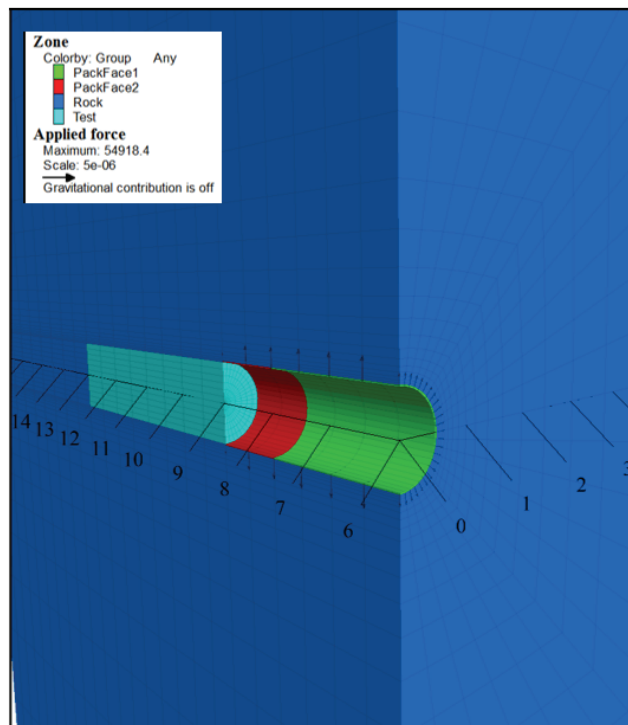


**Figure 4-13: Illustration of the Two Packer Pressure Application Zones (Applied Force is in Newtons)**

## 4.4 RESULTS AND DISCUSSION

In this section the results of the geomechanical modelling on the development of the EDZ, the changes in permeability during the simulation, the fit between measured and modeled test zone pore pressures, and the potential for general application in a repository setting are discussed.

### 4.4.1 Excavation Damage Zone Development

As described in Section 4.2.1, the extent of the excavation damaged zone (EDZ) was evaluated based on the plastic failure state from the UJM. The failure modes in the UJM are as follows: (1) no failure; (2) shear failure in the intact rock; (3) tension failure in the intact rock; (4) shear failure in the bedding plane; (5) tension failure in the bedding plane. Figure 4-14 shows the model predicted damage zone and compares it to the laser scan of the tunnel performed following the excavation. Damage is more severe where multiple failure modes overlap. Results show a good agreement between the predicted and the observed distribution of the EDZ. In particular, the locations where multiple failure modes overlap correspond well to locations where breakouts in the tunnel wall were observed.

Generalizing from this model, if pore pressure were sufficiently high, this could enhance damage and expand the EDZ. Stresses applied to the tunnel wall, such as the packer pressure, partially support the wall and reduce the degree of damage and the permeability. The action of the packer in the HG-A experiment is somewhat analogous to the effect of a swelling clay-based seal in a repository setting.

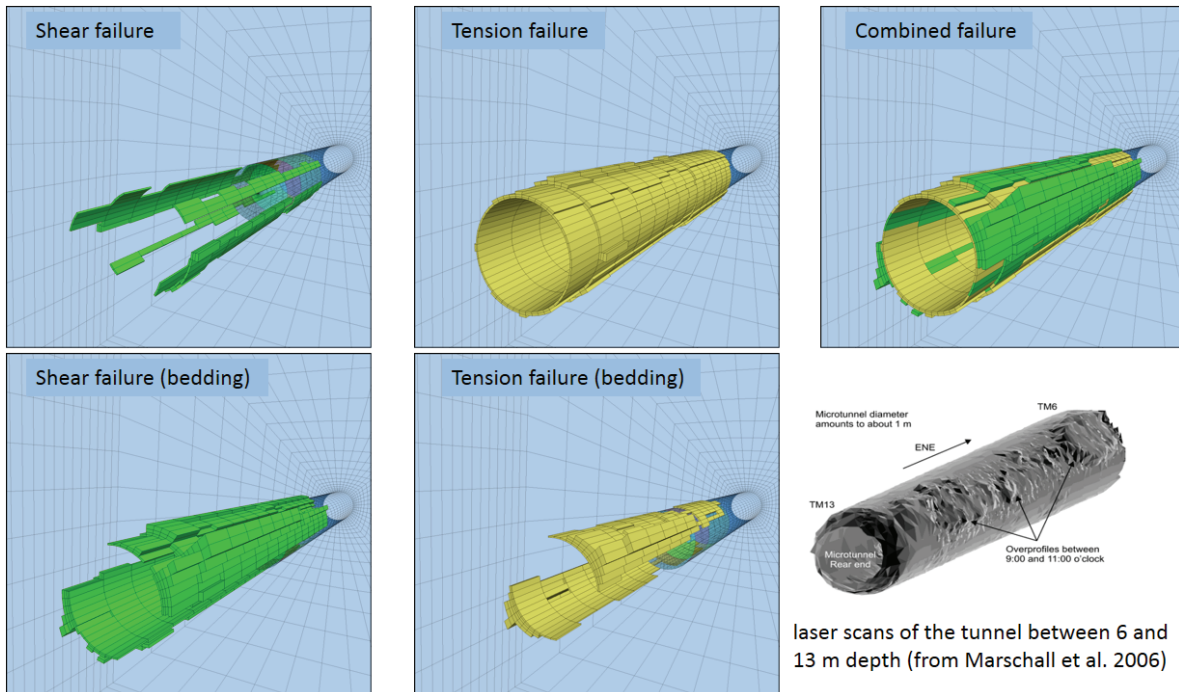


**Figure 4-14: Four Failure Modes Delineating the EDZ Extents Compared with a Laser Scan of the Tunnel Wall Following Excavation**

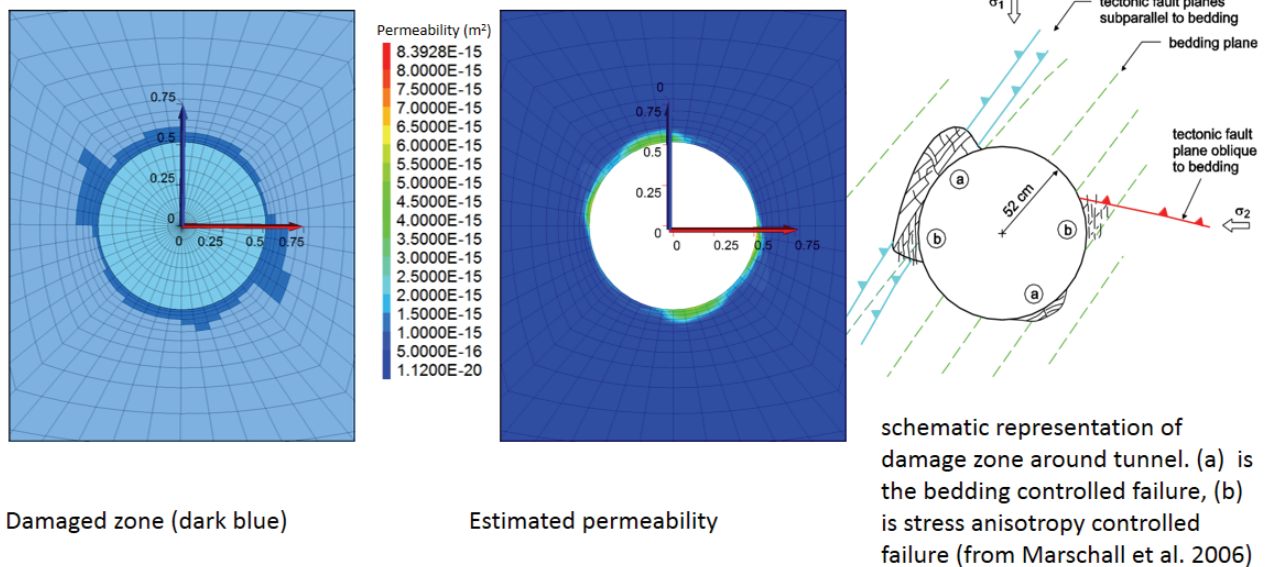
#### 4.4.2 Changes in Permeability

This section discusses the model predictions of changes in EDZ permeability, EDZ permeability distribution, and packer-wall interface permeability.

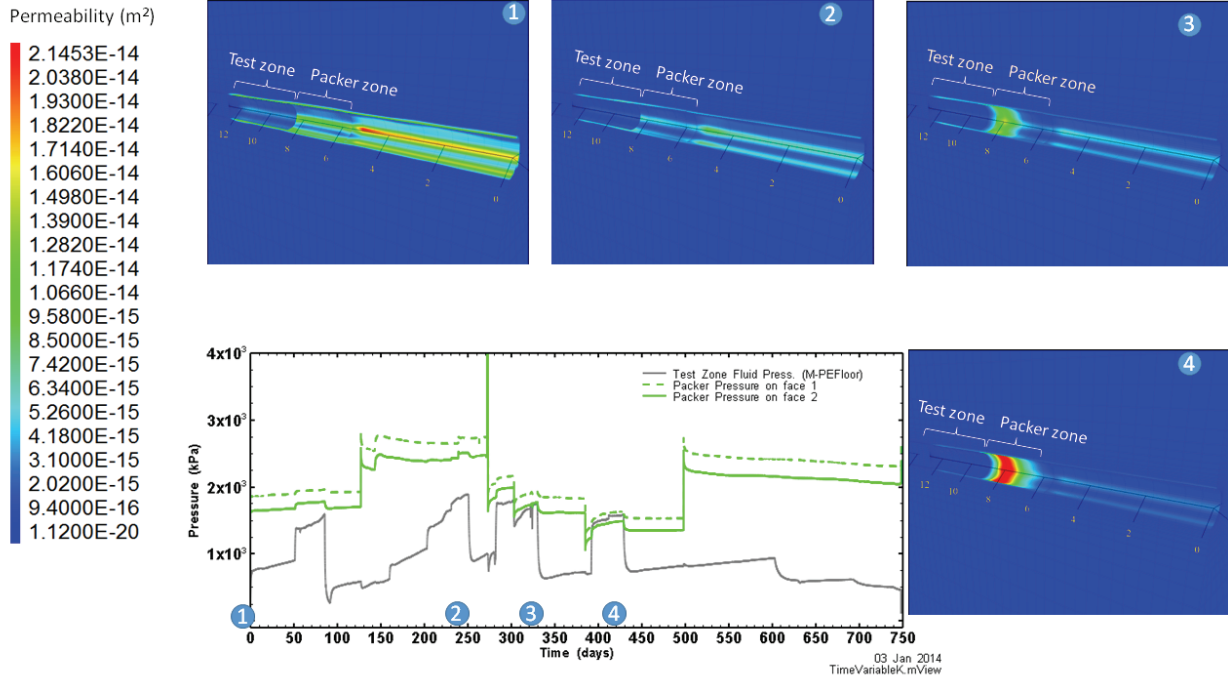
##### 4.4.2.1 EDZ

Figure 4-15 shows a cross section through the HG-A tunnel. The first panel in Figure 4-15 shows the estimated extent of the damage zone resulting from the combination of all failure modes (shear and tension failure in both intact rock and on the weak bedding plane). The predicted damage zone is qualitatively similar in both orientation and extent to a schematic representation of the damage zone prepared by Marschall et al. (2006). The second panel shows the estimated change in permeability as a result of the damage state. Where multiple modes of failure are predicted the permeability increase is greater.

Figure 4-16 shows the estimated EDZ permeability at four times. The EDZ permeability shown in this figure is a function effective stress (which changes mainly due to variation in packer pressure) and time dependent permeability decay due to swelling on fracture faces in the EDZ (self-healing). The permeability distribution at time (1) is due to stress relaxation caused by tunneling. As time progresses (times (2), (3), and (4)) the permeability in the EDZ adjacent to the test zone and the lined zone (cased zone) steadily decay. Adjacent to the packer, increased permeability is observed at times (3) and (4). This permeability increase is caused by reduced effective stress as the packer pressure drops and water pressure increases as shown in the bottom left figure (reproduced from Figure 4-6).



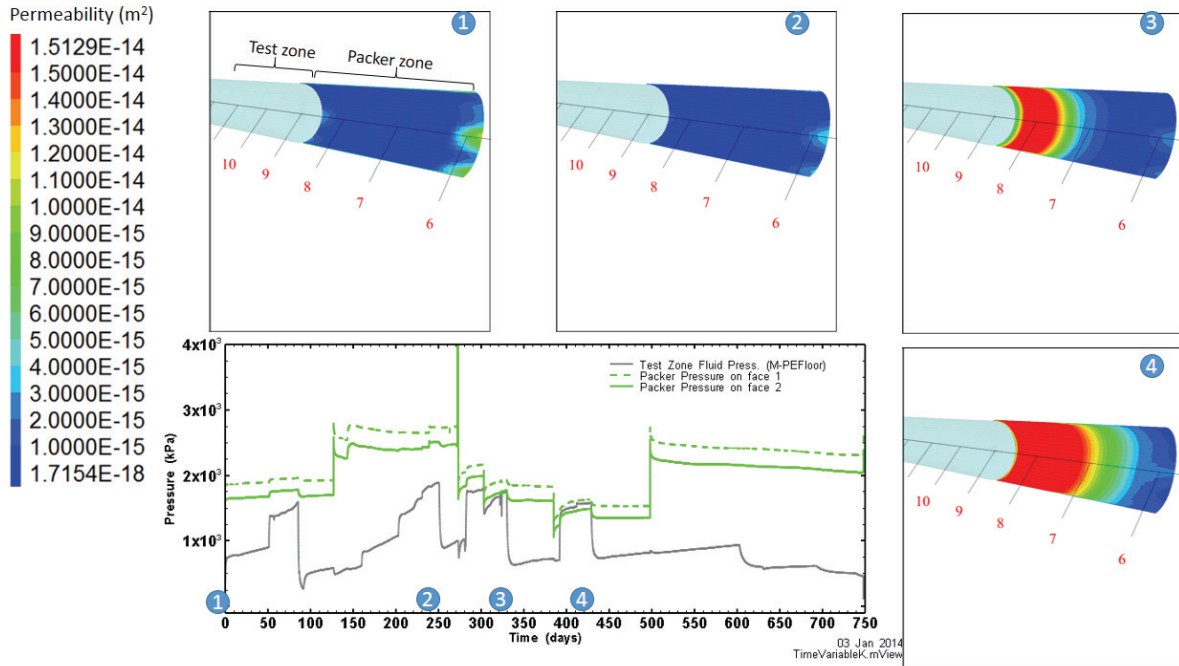
**Figure 4-15: Damaged Zone and the Estimated Change in Permeability Compared with the Schematic Representation of the Damaged Zone from Marschall et al. (2006)**



**Figure 4-16: Estimated Permeability of the EDZ and Its Changes with Time**

#### 4.4.2.2 Packer-Rock Interface

During the course of the HG-A experiment the effective stress reached minimum values at roughly 325 days and 425 days due to reducing the packer pressure and increasing the water pressure, simultaneously. Figure 4-17 shows the time variation in the packer-rock interface permeability estimated using Equation (12). The estimated permeability of the packer-rock interface increased at time (3) and (4) as a result of reduced effective stresses.



Note: Red numbers indicate depth along tunnel, in metres.

**Figure 4-17: Estimated Permeability of the Packer-Rock Interface at Four Times**

#### 4.4.3 Test Zone Pressure

Conceptually, this model simulated the hydro-mechanical behaviour of the system, including, the field stresses, excavation process, damage process, swelling process, packer performance and injection of water. In general, the simulated pressures compare well with the measured pressures in the test zone as shown in Figure 4-18 and Figure 4-19. More time spent on parametric fitting could produce better results.

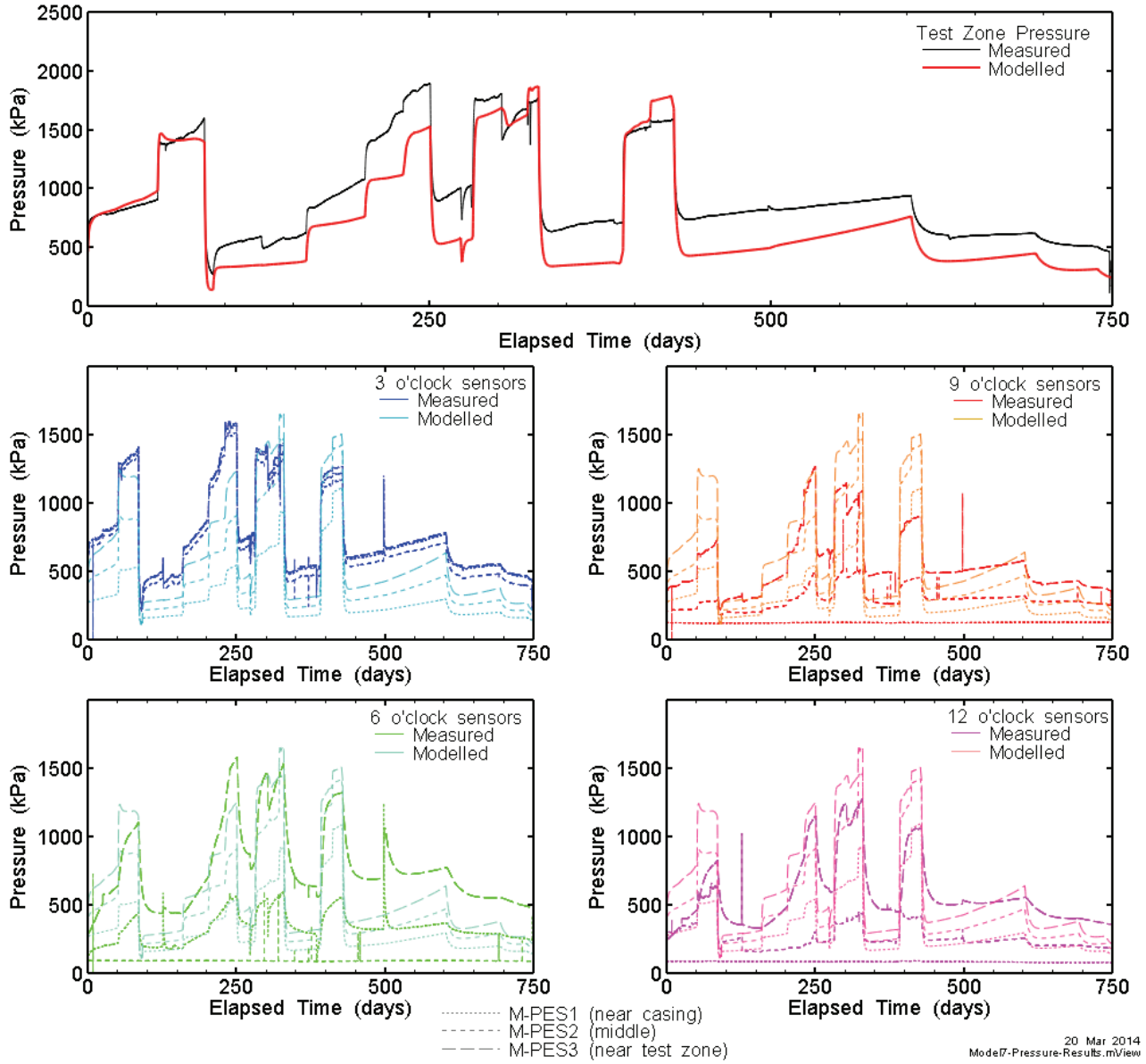


**Figure 4-18: Calculated Water Pressure at the Test Zone Compared with the Measured Pressure**

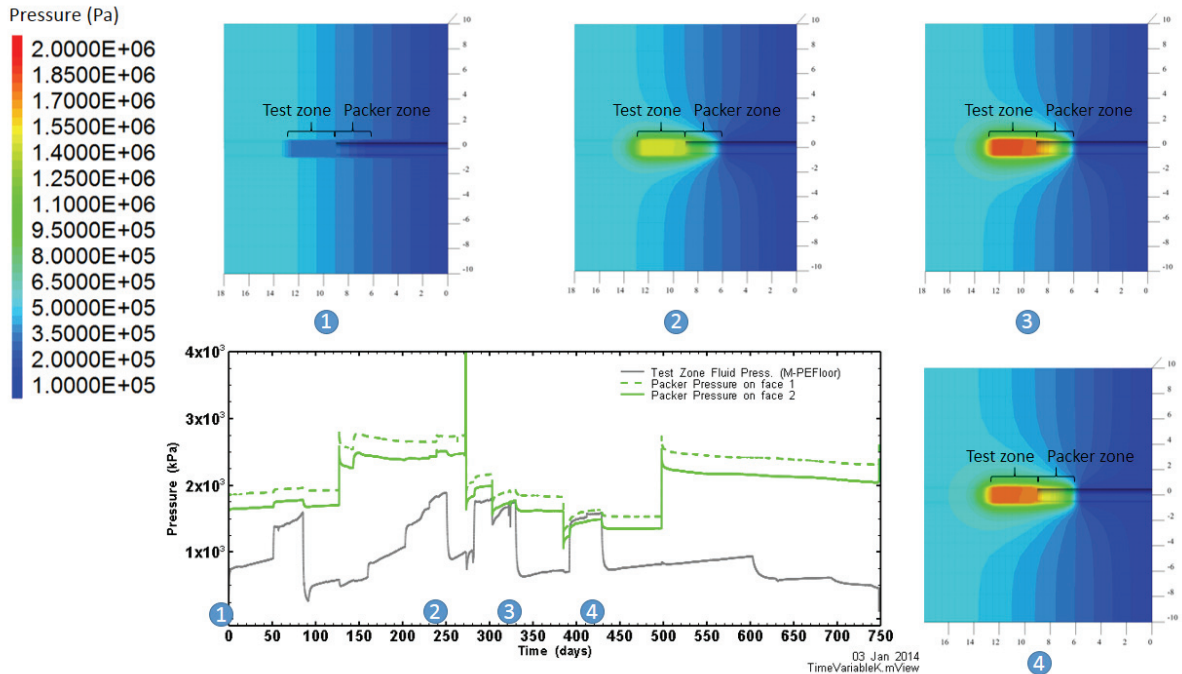


**Figure 4-19: 2D Cross Section of Calculated Water Pressure at Different Times**

#### 4.4.4 Discussion

The permeability of the EDZ controls the pressurization curve of the test zone. There are a number of distinct hydromechanical processes occurring in the EDZ, namely damage (plastic deformation) causing fracturing, effective stress changes opening and closing fractures and the packer-wall interface, and self-healing of fractures caused by swelling of clay minerals on or near the fracture faces. It is the combination of these processes that produces the overall behaviour of the system, and all key processes should be considered in the hydromechanical model for calculating the evolution of EDZ permeability.

First, we used the rock mechanical model to calculate the extent and degree of damage (plastic deformation) in the rock surrounding the tunnel. This part of the analysis was based on laboratory measurements of rock mechanical properties such as Young's Modulus, Poisson's ratio, and Mohr-Coulomb friction angle, and on credible estimates of the in-situ stress tensor. The damage distribution was calculated using parameters independent of the field-test, and resulted in a plausible damage distribution, qualitatively similar to the distribution in the HG-A tunnel, as characterized by laser-scans of the tunnel interior which measured the distribution of borehole breakouts.

There is currently no generally applicable rule to convert damage to permeability. To calculate the damage induced permeability of the EDZ, it was necessary to calibrate the damage-permeability equation (Equation (9), parameter  $B$ ). Permeability of the EDZ is not only a function of damage. As the packer pressure and test zone pressures changed during the test, the effective stress and thus the permeability of fractures in the EDZ also changed. Once again, stress-permeability coupling is difficult to determine *a priori*, as it is a function of fracture geometry, failure mode, mechanical restraints, and basic rock mechanical properties. The

permeability of single fractures in laboratory test specimens varies widely, even in rocks with similar bulk elastic properties (See Figure 4-5). In general, however, fractures become stiffer at increasing confining stresses, reducing the degree of fracture wall deformation and the resulting changes in permeability for a given stress increment. The exponential form of Equation (9) reflects this generally expected behavior, as does Equation (12). The calibration parameters controlling stress-permeability coupling were altered to improve the fit between modelled and measured test zone permeabilities.

Finally, the evolution of the EDZ due to swelling and self-healing of the fracture walls should be included in the model. An exponential decay function for reducing permeability with time has been observed in laboratory-scale experiments, and this form was adopted for Equation (11). Once again, the rate of decay was varied to improve the fit of the model.

The combination of these functions produced a reasonably good fit between modelled and measured test zone pressures (Figure 4-18). However, given the large number of calibration parameters, it is not reasonable to assume that our calibrated parameter set provides a unique solution. Indeed, due to long model runtimes, relatively little effort was spent optimizing the various parameters and the fit could probably be greatly improved. A better fit is very likely possible, but would not tell us more than this model does. What this model does tell us is that combining an elasto-plastic damage model with a relatively simple stress-permeability coupling function was able to reproduce the experimental behaviour to a reasonable degree. In other lithologies where swelling minerals are not present, or the leakage along the sealing-system interface was not probable, the number of functions and calibration parameters could be significantly reduced. Although it is difficult to say in advance what the damaged-zone permeability is likely to be, the calibrated EDZ permeability evolution is consistent with other in-situ experiments on EDZ at Mont Terri (Bernier et al. 2007).

## 5. CONCLUSIONS

This technical report presents our modelling of the HG-A experiment, as part of FORGE WP 4.3. The aims of this study were to improve the understanding of gas and water flow in the EDZ of a tunnel in Opalinus clay, to validate current modeling approaches and codes (T2GGM), and to develop novel methods for modelling the EDZ.

The initial modelling using T2GGM showed that it is not possible to reproduce the experimental results of the hydraulic test (from January 2008 to April 2010) with a model using constant EDZ permeability. It seems clear that the permeability of the EDZ during the first 839 days of the HG-A experiment was affected by two distinct processes: (1) ongoing swelling of the damaged rock in the presence of water led to healing of fractures, which resulted in a steady reduction in the permeability of the damaged zone; and (2) hydromechanical coupling as changes in pore pressure and confining stress (packer pressure) caused rapid changes in permeability.

Two approaches for estimating the changes in permeability during the hydraulic test were developed and are presented in this report. The first approach is a simple analysis of pressure data and back-calculation of permeability as a function of time. To test the impact of the changing permeability on the modelled pressure, a new algorithm was added to T2GGM that allows the application of a time-varying permeability. This approach provided a very good fit to modelled pressures, but cannot be considered predictive in any way.

By the end of the multi-rate hydraulic test, the properties of the EDZ were approaching a steady state. It was possible to successfully model Gas Tests 1 and 2 using constant permeabilities for the permeable EDZ channel, although the permeability did change slightly between tests. Gas Test 3 required minor permeability variations during the test to optimize the model fit. The fact that the properties needed to be changed between tests is likely due to trapped gas in the EDZ, possibly affecting the relative permeability. The gradual decay of packer pressures may also have impacted EDZ permeability. There is strong evidence that the gas entered the EDZ through a preferential flow pathway in the EDZ, located between roughly the 9 o'clock and 10 o'clock position in the tunnel.

The second approach to estimating the EDZ permeability is the coupled hydro-mechanical approach, in which the EDZ development is predicted based on plastic deformation and permeability is modified for the damaged zones based on a reasonable estimate of the form of the stress-permeability coupling relationship and calibration of empirical parameters. This approach may be considered predictive in terms of modelling the extent and geometry of the EDZ. The distribution of damage around the HG-A tunnel as predicted by the model corresponds well to available measurements of damage from laser scans of the tunnel walls post-excavation, providing tangible evidence that the model is reliable. This rather good qualitative fit is not a result of careful calibration, but rather the application of geomechanical first principles, laboratory measurements of geomechanical parameters and parameter anisotropy, and estimates of the local geomechanical stress state.

To calculate the damage-induced permeability, it was still necessary to calibrate a number of empirical parameters. With limited calibration, this approach was able to reproduce measured test zone pressures to a reasonable degree of accuracy. It may be possible to design laboratory experiments to provide the probable range of the permeability increase under a given damage scenario, making this hydro-mechanical model a valuable tool for predicting long-term permeability change in a repository setting.

There is scope for further refinements to the HG-A hydro-mechanical model. These could include further refinement of the damage-permeability relationship, separating the applied packer pressure into a larger number of zones (rather than averaging), and calculating the effect of changing porosity on pore pressures, especially in the test zone.

Contrary to common conceptual models of EDZ distribution in a repository, the EDZ predicted by the hydromechanical model (and required to fit the two-phase flow model of the gas injection tests) is relatively thin and heterogeneous. Permeability is not uniformly distributed around the circumference of the tunnel, but localized in channels. The extent of the EDZ is very much a function of the magnitudes and orientation of the local stress tensor and the fabric of the rock. While this model used a homogenous (and anisotropic) distribution of stresses and rock properties, it produced a heterogeneous EDZ. Local variations in stress or rock fabric could further amplify the degree of EDZ heterogeneity. In a different stress environment, with a different type of rock, the extent of the EDZ could be different.

## REFERENCES

- Bernier, F., X.L. Li, W. Bastiaens, L. Ortiz and M. Van Geet. 2007. SELFRAC – Fractures and Self-healing within the Excavation Disturbed Zone in Clays – Final Report. 64 P., 5th EURATOM Framework Programme, Brussels (EU-Commission).
- Bethke, C.M. and T.F. Corbet. 1988. Linear and Nonlinear Solutions for One-dimensional Compaction Flow in Sedimentary Basins. *Water Resources Research*, 24, 461–467.
- Blümling, P. and H. Konietzky. 2004. Calibration and Verification of a Constitutive Law for Opalinus Clay - Results from Laboratory and In-situ Tests. 2nd Colloquium “Rock Mechanics – Theory and Practice”, March 2004, *Mitteilungen für Ingenieurgeologie und Geomechanik* (6), pp 89-95, Vienna.
- Bock, H. 2001. RA Experiment Rock Mechanics Analyses and Synthesis: Conceptual Model of the Opalinus Clay. Mont Terri Technical Report 2001-03, Geotech. Inst. Ltd. Bern, Switzerland.
- Bock, H., B. Dehandschutter, C. D. Martin, M. Mazurek, A. De Haller, F. Skoczylas and C. Davy. 2010. Self-sealing of Fractures in Argillaceous Formations in the Context of Geological Disposal of Radioactive Waste Review and Synthesis Report. OECD NEA 6184. Waste Management. Paris,France: NEA OECD.
- Corkum, A.G. and C.D. Martin. 2007. Modelling a Mine-by Test at the Mont Terri Rock Laboratory, Switzerland. *Int. J. Rock Mech. Min. Sci.*, 44, 846-885.
- Corkum, A.G. and C.D. Martin. 2008. Technical Memorandum: HG-A/Phase 13 Experiment: Evaluation of Biaxial Stressmeters. Ref: ICG08-2509-19TMD, Itasca Consulting Group. Minneapolis, Minnesota.
- Das, B. 2007. *Fundamentals of Geotechnical Engineering*. Cengage Learning, 247.
- Davy, C., F. Skoczylas, J.D. Barnichon and P. Lebon. 2007. Permeability of Macro-cracked Argillite under Confinement: Gas and Water Testing. *Physics and Chemistry of the Earth* 32, 667-680.
- Itasca Consulting Group Inc. 2012. *FLAC3D (Fast Lagrangian Analysis of Continua)*. Version 5.01.
- Lanyon, G.W., P. Marschall, T. Trick, R. de la Vaissiere, H. Shao and H. Leung. 2009. Hydromechanical Evolution and Self-Sealing of Damage Zones around a Microtunnel in a Claystone Formation of the Swiss Jura Mountains. Conference Proceedings from the 43rd US Rock Mechanics Symposium and 4th U.S.-Canada Rock Mechanics Symposium, held in Asheville, NC, June 28 to July 1, 2009.
- Lanyon, G.W. 2011a. Personal communication by email to R. Walsh on 27 May 2011 from G.W. Lanyon of Fracture Systems Limited (Nagra consultant for HG-A project).

- Lanyon, G.W. 2011b. Personal communication by email to J. Avis on 7 April 2011 from G.W. Lanyon of Fracture Systems Limited (Nagra consultant for HG-A project), providing the project ftp site and data packages.
- Lanyon, G.W. 2012. HG-A (Gas Path Through Host Rock and Along Seals) Experiment: Preliminary Interpretation of Gas Injections during Phase 15 &16. Mont Terri TN 2010-40. Fracture Systems Ltd, St Ives, Cornwall, United Kingdom.
- Marschall, P., S. Horseman, and T. Gimmi. 2005. Characterisation of Gas Transport Properties of the Opalinus Clay, a Potential Host Rock Formation for Radioactive Waste Disposal. *Oil and Gas Science and Technology*, 60 (1), 121-139.
- Marschall, P., M. Distinguin, H. Shao, P. Bossart, C. Enachescu and T. Trick. 2006. Creation and Evolution of Damage Zones around a Microtunnel in a Claystone Formation of the Swiss Jura Mountains. Conference Proceedings from the 2006 SPE International Symposium and Exhibition on Formation Damage Control held in Lafayette, L.A., 15–17 February 2006, SPE Paper 98537.
- Martin, C.D. and G.W. Lanyon. 2003. Measurement of In-situ Stress in Weak Rocks at Mont Terri Rock Laboratory. *International Journal of Rock Mechanics and Mining Sciences*, 40, Issue 7-8, 1077-1088.
- Person, M., V. Bense, D. Cohen and A. Banerjee. 2012. Models of Ice-Sheet Hydrogeologic Interactions: A Review. *Geofluids* 12, 58-78.
- Popp, T., K. Salzer and W. Minkley. 2008. Influence of Bedding Planes to EDZ-evolution and the Coupled HM Properties of Opalinus Clay. *Physics and Chemistry of the Earth* 33, S374-S387.
- Pruess, K., C. Oldenburg and G. Moridis. 1999. TOUGH2 User's Guide, Version 2.0. Lawrence Berkeley National Laboratory LBNL-43134. Berkeley, USA.
- Rutqvist, J. and C.F. Tsang. 2003. TOUGH-FLAC: A Numerical Simulator for Analysis of Coupled Thermal-Hydrologic-Mechanical Processes in Fractured and Porous Geological Media under Multi-phase Flow Conditions. Conference Proceedings from the TOUGH2 Symposium 2003, Lawrence Berkeley National Laboratory, Berkeley, California, May 2003.
- Suckling, P., J. Avis, N. Calder, P. Humphreys, F. King and R. Walsh. 2012. T2GGM Version 3.1: Gas generation and Transport Code. Nuclear Waste Management Organization Report NWMO TR-2012-23. Toronto, Canada.
- Walsh, R., C. McDermott and O. Kolditz. 2008. Numerical Modeling of Stress-Permeability Coupling in Rough Fractures. *Hydrogeology Journal*, 16(4), 613-627.
- Walsh, R., N. Calder and J. Avis. 2012. A Simple Implementation of 1D Hydromechanical Coupling in TOUGH2. Conference Proceedings from the TOUGH2 Symposium 2012, Lawrence Berkeley National Laboratory, Berkeley, California, September 2012.

Zang A. and O. Stephansson. 2010. Stress Field of the Earth's Crust. Springer, Heidelberg, Germany.

Zhang L. and D.G. Fredlund. 2003. Characteristics of Water Retention Curves for Unsaturated Fractured Rocks. Conference Proceedings from the Second Asian Conference on Unsaturated Soils, Osaka, Japan, April 15-17, 2003.

## APPENDIX A: SENSOR LOCATIONS

Table A-1: Locations and Descriptions of Relevant Sensors in the Microtunnel

Name	HG-A Microtunnel Sensors Description	Units	Radial Coordinates			Cartesian Coordinates		
			R (m)	Angle	Y (m)	X (m)	Y (m)	Z (m)
M-PES1-3h	Mega packer piezometer section 1 at 3 o'clock	kPa	0.50175	90	6.627	0.502	6.627	0.000
M-PES1-6h	Mega packer piezometer section 1 at 6 o'clock	kPa	0.50175	180	6.627	0.000	6.627	-0.502
M-PES1-9h	Mega packer piezometer section 1 at 9 o'clock	kPa	0.50175	270	6.627	-0.502	6.627	0.000
M-PES1-12h	Mega packer piezometer section 1 at 12 o'clock	kPa	0.50175	360	6.627	0.000	6.627	0.502
M-PES2-3h	Mega packer piezometer section 2 at 3 o'clock	kPa	0.50175	90	7.614	0.502	7.614	0.000
M-PES2-6h	Mega packer piezometer section 2 at 6 o'clock	kPa	0.50175	180	7.614	0.000	7.614	-0.502
M-PES2-9h	Mega packer piezometer section 2 at 9 o'clock	kPa	0.50175	270	7.614	-0.502	7.614	0.000
M-PES2-12h	Mega packer piezometer section 2 at 12 o'clock	kPa	0.50175	360	7.614	0.000	7.614	0.502
M-PES3-3h	Mega packer piezometer section 3 at 3 o'clock	kPa	0.50175	90	8.601	0.502	8.601	0.000
M-PES3-6h	Mega packer piezometer section 3 at 6 o'clock	kPa	0.50175	180	8.601	0.000	8.601	-0.502
M-PES3-9h	Mega packer piezometer section 3 at 9 o'clock	kPa	0.50175	270	8.601	-0.502	8.601	0.000
M-PES3-12h	Mega packer piezometer section 3 at 12 o'clock	kPa	0.50175	360	8.601	0.000	8.601	0.502
M-TPS1-4h	Mega packer total pressure section 1 at 4 o'clock	kPa	0.50175	120	7.850	0.435	7.850	-0.251
M-TPS1-8h	Mega packer total pressure section 1 at 8 o'clock	kPa	0.50175	240	7.863	-0.435	7.863	-0.251
M-TPS1-12h	Mega packer total pressure section 1 at 12 o'clock	kPa	0.50175	360	8.362	0.000	8.362	0.502
M-TPS2-4h	Mega packer total pressure section 2 at 4 o'clock	kPa	0.50175	120	8.840	0.435	8.840	-0.251
M-TPS2-8h	Mega packer total pressure section 2 at 8 o'clock	kPa	0.50175	240	8.870	-0.435	8.870	-0.251
M-TPS2-12h	Mega packer total pressure section 2 at 12 o'clock	kPa	0.50175	360	8.873	0.000	8.873	0.502
M-PEFloor	Test Section piezometer in ceiling	kPa	0.50175	180	12.000	0.000	12.000	-0.502
M-PECeiling	Test Section piezometer in floor	kPa	0.50175	360	12.000	0.000	12.000	0.502

**Table A-2: Locations and Descriptions of Relevant Sensors in the Observation Boreholes**

Name	Borehole Sensors		Units	Start Coordinates			End Coordinates		
	Description			X (m)	Y (m)	Z (m)	X (m)	Y (m)	Z (m)
B-A02PE1	HG-A2 interval 1 pressure		kPa	-0.090	12.191	2.171	-0.100	13.691	2.192
B-A02PE2	HG-A2 interval 2 pressure		kPa	-0.071	9.191	2.127	-0.087	11.691	2.163
B-A02PE3	HG-A2 interval 3 pressure		kPa	-0.045	5.192	2.069	-0.068	8.691	2.120
B-A02PA1	HG-A2 packer pressure 1		kPa	-0.087	11.691	2.163	-0.090	12.191	2.171
B-A02PA2	HG-A2 packer pressure 2		kPa	-0.068	8.691	2.120	-0.071	9.191	2.127
B-A02PA3	HG-A2 packer pressure 3		kPa	-0.042	4.692	2.061	-0.045	5.192	2.069
B-A03PE1	HG-A3 interval 1 pressure		kPa	-1.995	12.012	-0.235	-2.116	13.527	-0.262
B-A03PE2	HG-A3 interval 2 pressure		kPa	-1.756	9.022	-0.181	-1.955	11.514	-0.226
B-A03PE3	HG-A3 interval 3 pressure		kPa	-1.437	5.035	-0.110	-1.716	8.524	-0.172
B-A03PA1	HG-A3 packer pressure 1		kPa	-1.955	11.514	-0.226	-1.995	12.012	-0.235
B-A03PA2	HG-A3 packer pressure 2		kPa	-1.716	8.524	-0.172	-1.756	9.022	-0.181
B-A03PA3	HG-A3 packer pressure 3		kPa	-1.397	4.537	-0.101	-1.437	5.035	-0.110
B-A08PE1	HG-A8 mini-piezometer pressure		kPa	3.188	3.429	0.124	2.886	3.706	0.111
B-A09PE1	HG-A9 mini-piezometer pressure		kPa	2.973	5.728	0.119	2.827	5.864	0.111
B-A10PE1	HG-A10 mini-piezometer pressure		kPa	4.260	6.540	-3.163	4.151	6.634	-3.301
B-A11PE1	HG-A11 mini-piezometer pressure		kPa	3.360	9.462	0.008	3.214	9.598	0.001
B-A12PE1	HG-A12 mini-piezometer pressure		kPa	5.042	9.848	-4.355	4.935	9.943	-4.495
B-A13PE1	HG-A13 mini-piezometer pressure		kPa	3.510	13.028	-0.153	3.359	13.159	-0.160
B-A24PE1	HG-A24 mini-piezometer pressure		kPa	3.451	12.202	-2.145	3.306	12.330	-2.197
B-A25PE1	HG-A25 mini-piezometer pressure		kPa	3.393	12.253	1.985	3.248	12.381	2.037

## APPENDIX B: VAN GENUCHTEN MODEL

To model two phase flow, the capillary pressure and relative permeability functions are required. In this work, the capillary pressure and relative permeability curves are represented using the Van Genuchten equations:

$$P_c = -\frac{1}{\alpha} [S_{ec}^{-1/m} - 1]^{1/n}$$

$$S_{ec} = \frac{S_l - S_{lr}}{1 - S_{lr}}$$

$$k_{rl} = S_{ek}^{1/2} [1 - (1 - S_{ek}^{1/m})^m]^2$$

$$k_{rg} = 1 - k_{rl}$$

$$S_{ek} = \frac{S_l - S_{lr}}{1 - S_{lr} - S_{gr}}$$

Where:

- $P_c$  = the capillary pressure, Pa;
- $k_{rl}$  = the liquid phase relative permeability (ratio);
- $k_{rg}$  = the gas phase relative permeability (ratio);
- $S_{ec}$  = the effective saturation for the capillary pressure relationship (volume ratio);
- $S_{ek}$  = the effective saturation for the relative permeability relationship (volume ratio);
- $S_l$  = the liquid saturation (volume ratio);
- $S_{lr}$  = the residual liquid saturation (volume ratio), the liquid saturation below which liquid does not flow;
- $S_{gr}$  = the residual gas saturation (volume ratio), the gas saturation below which gas does not flow;
- $m$  = a van Genuchten fitting parameter (unitless);
- $n$  = a van Genuchten fitting parameter (unitless,  $n = 1/(1-m)$ ); and
- $\alpha$  = a van Genuchten fitting parameter,  $\text{Pa}^{-1}$ . The inverse of  $\alpha$  is analogous to the air entry pressure.